# DISORDER TO ORDER IN OSCILLATORY AND EXCITABLE SYSTEMS

A Dissertation
Presented to
The Academic Faculty

By

Noah DeTal

In Partial Fulfillment
of the Requirements for the Degree
Doctor of Philosophy in the
School of Physics

Georgia Institute of Technology

August 2021

© Noah DeTal 2021

**DISORDER TO ORDER IN OSCILLATORY AND EXCITABLE SYSTEMS**

Thesis committee:


Dr. Flavio Fenton, Advisor
School of Physics
*Georgia Institute of Technology*

Dr. Daniel Goldman
School of Physics
*Georgia Institute of Technology*

Dr. Kurt Wiesenfeld, Coadvisor
School of Physics
*Georgia Institute of Technology*

Dr. Hans Dierckx
Department of Mathematics
*Katholieke Universiteit Leuven*

Dr. Elizabeth Cherry
School of Computational Science
and Engineering
*Georgia Institute of Technology*



Date approved: July 23, 2021

## ACKNOWLEDGMENTS

For their continued inspiration and support, I would like to thank Flavio Fenton, Kurt Wiesenfeld, Hector Augusto Velasco-Perez, Shaun Eisner, and Vicki deTal.

## TABLE OF CONTENTS

## LIST OF TABLES

## LIST OF FIGURES

## SUMMARY

In this thesis, two problems involving the macroscopic ordering of coupled nonlinear elements are studied. The first problem involves analyzing a synchronizing transition in a population of coupled oscillators. Synchronization of the oscillators in this model corresponds to coherent propagation of solitary waves in a nonlinear Schrödinger equation. The second problem concerns the elimination of chaotic fibrillatory dynamics in excitable cardiac tissue. In the fibrillatory state, reentrant spiral waves of electrical activity entrain the excitable cells and interrupt the healthy heart rhythm. By appealing to the topological structure of excitable dynamics, conditions are derived for the stimulated elimination of spiral waves and associated fibrillation. Insights from this topological framework are then applied to the optimization of a novel low-energy multi-pulse defibrillation scheme.

# CHAPTER 1
# INTRODUCTION AND BACKGROUND

## 1.1 Introduction

Oscillatory [1] and excitable [2] media are classic examples of systems in which emergent behavior arises from the interactions between individual nonlinear elements. In oscillatory systems, individual elements exhibit persistent periodic behavior the timing of which is influenced by its coupled neighbors. In excitable systems, elements undergo large cycles of activation but eventually return to a stationary rest state. However, neighboring activations can cause them to reexcite. Significant theoretical progress has been made for both oscillatory and excitable systems by appealing to differences in time scales [3, 4, 5]. Oscillators tend to rapidly approach their natural limit cycles with only the overall phase of oscillation perturbed by neighboring elements. Similarly, excitable systems contain a pair of slow manifolds which the system can rapidly jump between. Depending on the details of the interactions between elements, macroscopic behavior in both system types can range from disordered to ordered; in applications, typically one or the other is desired. In this thesis, two problems of this nature are discussed. In the first, the generation of nonlinear optical waves is explored in an underlying phase model. Synchronization of the oscillators in this model is a necessary condition for stable wave propagation. The second problem concerns the persistence of irregular electrical activation in excitable cardiac tissue. The disordered fibrillating state is characterized by emergent topological defects known as spiral waves. Spiral waves provide sustained periodic activation in the otherwise nonoscillatory medium and must be eliminated to reestablish a healthy rhythm.

## 1.2 Background

### 1.2.1 Phase reduction, coupled oscillators, and synchronization

Mathematically, an oscillator is simply any system of ordinary differential equations (ODEs) that supports a stable limit cycle. A periodic phase can be assigned to the limit cycle to track its periodic progression [6]. When an oscillator is perturbed (e.g. by coupling), it becomes displaced from its limit cycle and phase is no longer sufficient to describe the system's state. However, if the system converges sufficiently quickly back to the limit cycle (i.e. the leading Floquet multiplier is small), the effect of the perturbation can be approximated as merely shifting the oscillator's phase. The rigorous application of this approximation is known as phase reduction; it reduces the dynamics of the original $N$-dimensional ODE to a one-dimensional problem solely in terms of phase evolution [1]. The key ingredient to this theory is the phase response function, which gives the approximate phase shift due to perturbation at every possible phase [6].

One of the most successful applications of phase reduction theory is systems of coupled oscillators. When nearly identical oscillators are coupled globally, sufficiently strong interaction often leads to macroscopic synchronization. In the synchronized state, every oscillator proceeds with almost identical phase [1]. The most famous system demonstrating such a synchronizing transition is the exactly solvable Kuramoto model [7]. Synchronization is highly desirable in certain engineered systems for which cooperation is required between many components. For example, synchronization in Josephson junction arrays allows for high-power, high-frequency signal output [8]. In Chapter 2 of this thesis, a reduced phase model of nonlinear wave generation is shown to undergo a synchronizing transition which allows for coherent wave propagation in the original problem. This model shares many structural properties with the Kuramoto model, but has a unique ternary coupling between oscillators.

In biological contexts, oscillatory and excitable elements often interact via diffusive (or

nearest neighbor) coupling as opposed to global (or all-to-all) coupling [2, 1]. Without instantaneous coupling across all elements, oscillator synchronization is no longer possible. However, an emergent type of coherence is still possible in the form of propagating phase waves. The complex spatiotemporal dynamics of diffusive oscillatory media can be understood quite naturally in terms of individual oscillator phase and phase reduction theory [1]. This is true even for the case of spiral waves, in which a phase singularity near the center of rotation necessarily violates the phase representation [9]. As we shall discuss next, excitable media is much more subtle to characterize because it lacks an intrinsic local representation such as phase.

### 1.2.2 Excitable media, spiral waves, and cardiac dynamics

In isolation, excitable elements merely tend to their stable rest state. If perturbed beyond a threshold, they may become temporarily activated, leading to a large, rapid transient response before ultimately approaching a stable fixed point. Excitable ODE systems typically have an explicit time scaling parameter $\epsilon$ that ensures one variable evolves much faster than the others [10]. Planar systems in particular have a single fast variable and slow variable, respectively. In the singular limit of vanishing $\epsilon$, the fast variable becomes entrained to the slow variable except during drastic jumps characterizing activation or deactivation [3].

When many excitable elements are coupled in a spatially extended continuum known as an excitable medium, a plethora of emergent behaviors are made possible [2]. The simplest coupled behavior is the propagation of waves, in which excitation spreads from element to element at a constant velocity. An exceedingly important emergent property of such propagation is the notion of refractoriness. Elements in the rest state are readily excited by their neighbors. Upon activation, however, there is a finite time before the element may reactivate. This refractory period is necessary for unidirectional propagation and allows for differentiation between wave front and wave back. Refractoriness can be made mathematically precise by once again considering the limit of vanishing $\epsilon$. Standard

singular perturbation theory then shows that the velocity of an excited front is set by the slow variable [3]. If the slow variable is sufficiently far from its rest value, the resulting front's velocity will be negative; this results in a contracting rather than expanding front, and no resulting propagation. Refractoriness can thus be defined in terms of the value of the slow variable, and in general the state of an excitable element may be classified as excited, refractory, or resting. It is important to note, however, that this classification is strictly emergent, and isolated elements cannot rigorously be described this way.

Under ordinary conditions, linearly propagating excitation waves are transient. When they extinguish at a domain boundary, the medium will return to the rest state until reactivated by an external stimulus. However, a persistent excitation wave can form when an excited front of a wave meets a refractory back [9]. This ouroboric configuration is known as a spiral wave and continually emits radial excitation waves in a spiral pattern as it rotates around the excited-refractory intersection at its core [2]. Spiral waves are a form of topological defect and as such have strong constraints on how they can form or dissipate. Once formed, a spiral wave will invade the entire excitable domain and induce periodic excitation in every element. This periodic behavior is starkly different than that of oscillatory media, in which the oscillation is intrinsic to the individual elements themselves. Nevertheless, spiral waves in excitable media can appear virtually indistinguishable from spirals in oscillatory media.

One of the most studied examples of a real excitable medium is cardiac tissue in the myocardium. Regular contraction of the heart is induced by waves of electrical activation in the underlying cardiac cells [11]. These waves are stimulated by oscillatory pacemaker cells in the sinoatrial node that dictate the frequency of activation. Deadly arrythmias can arise in the heart as a result of pathological configurations in the excitable medium. Fibrillation, in which the heart rapidly contracts in an irregular, incoherent fashion, has been increasingly linked to the presence of reentrant spiral waves [12, 13]. Once formed, spiral waves interrupt the natural driving rhythm of the pacemaker cells, replacing it with their

intrinsic rotational frequency. Spiral waves can also undergo instabilities that generate additional spiral waves, leading to a rapid runaway process that saturates the medium with fibrillating disorder [14]. Chapters 3 and 4 of this thesis explore methods of terminating the fibrillating state by eliminating the underlying spiral wave activity responsible. By appealing to the topological organization of excitable media in terms of excited and refractory regions, novel defibrillation strategies are proposed which for the first time target the underlying drivers of complexity directly.

# CHAPTER 2

# SYNCHRONIZATION BEHAVIOR IN A TERNARY PHASE MODEL

## 2.1 Introduction

[1] Mode locking, i.e. alignment of laser mode frequencies on an equidistant spectral grid, has long been known to be a requirement for pulsation in actively and passively mode-locked lasers [15, 16, 17]. Variants of the nonlinear Schrödinger equation (NLSE) that admit sharply peaked soliton pulses have successfully been used to model many types of mode locked lasers [18, 19, 20, 21]. The connection between mode locking (pulsation in the time domain) and the universal phenomenon of self-synchronization is evidenced by the alignment and synchronous oscillation of Fourier modes in the frequency domain, see, e.g., [22, 23, 24]. Recently, this nexus was formally established through a phase model underlying spontaneous pulse formation in the damped and driven NLSE [25], also called the Lugiato-Lefever equation (LLE) [26].

Interestingly, this phase model is of a novel type within the realm of self-synchronization phenomena: the phases interact in triples rather than pairs. The ternary coupling is rooted in the physics of the nonlinear interaction; specifically, the conservation of energy and momentum in nonlinear four-wave mixing in optical Kerr resonators. In this Chapter, we treat the ternary phase model as a stand-alone model worthy of independent investigation from a nonlinear dynamical perspective. In particular, we explore the transitions to partial and complete synchronization, and compare the basic phenomenology to that of the Kuramoto model, the archetype of pairwise-interacting oscillator populations.

The Chapter is organized as follows. In section 2.2 we introduce the ternary phase

[1] Reproduced from N. DeTal, H. Taheri, and K. Wiesenfeld, "Synchronization behavior in a ternary phase model", Chaos: An Interdisciplinary Journal of Nonlinear Science 29, 063115 (2019) https://doi.org/10.1063/1.5097237, with the permission of AIP Publishing.

model and briefly review its relationship to the NLSE. In section 2.3, we present the results of numerical simulations showing the transition behavior for different choices of disorder, and compare this with the corresponding behavior of the Kuramoto model. In section 2.4 we construct a "thermodynamic limit" of the model and derive an expression we then use to calculate the order parameter quantifying synchronization. We end with a discussion of open questions.

## 2.2 Background

In this Chapter, we explore a disordered version of the following coupled oscillator equation [25]

$$\dot{\Delta}_j = \frac{K}{2N} \sum_{l=j-N}^{N} \sin(\Delta_l + \Delta_{j-l} - \Delta_j), \qquad ; \qquad j = 1, 2, \ldots, N \tag{2.1}$$

where $\Delta_j$ is the phase of the $j^{th}$ oscillator, and $K$ is the coupling constant. By definition, $\Delta_{-j} = -\Delta_j$. The equation bears some resemblance to the Kuramoto model [7]. We briefly review how Equation 2.1 comes about; full technical details can be found in Ref. [25].

Equation 2.1 governs the slow dynamics of the LLE in the strongly pumped limit. As first noted by Wen et al., in this limit, the dynamical evolution of the system proceeds in three successive steps, which can be captured by a systematic expansion in inverse powers of the pump amplitude [23]. On the fastest time scale, the pumped mode steady-state is established. On the intermediate time scale, mode pairs (symmetrically located about the pump frequency) grow via parametric amplification. Each mode pair evolves independently, reaching its steady state amplitude, and simultaneously a partial ordering of its phases such that $\phi_j + \phi_{-j} - 2\phi_0 = 0$. (Indices are chosen such that the pump index is zero.) It is during this intermediate time scale that a dense frequency comb is established; however, localized/pulsing dynamics emerges only on a still slower time scale, described

by Equation 2.1, during which the anti-symmetric parts of the phase pairs $\Delta_j = \phi_j - \phi_{-j}$ interact with each other. In the context of the LLE, $\Delta_j$ specifies a phase difference between modes. In this Chapter, we consider the set to be absolute phases of an oscillator population. The three-phase coupling of Equation 2.1 is the direct consequence of the cubic nonlinearity in the underlying wave equation. We note that phase models with three- and higher-fold couplings are not unheard of, and in fact arise generically in certain contexts [27].

Our first observation is that Equation 2.1 admits a family of perfectly synchronized states, given by

$$\Delta_j = \alpha \cdot j \tag{2.2}$$

for any constant $\alpha$. In the context of the micro-resonator problem, these states correspond to a spatially localized pulse propagating around the micro-resonator ring, and $\alpha$ determines the location of the optical pulse in the co-moving frame. This definition of synchronization is analogous to the situation in the Kuramoto model, in which the oscillators converge to an arbitrary phase

$$\theta_j = \beta. \tag{2.3}$$

For the ternary model, the oscillators will have identical phases if $\alpha = 0$, though there is nothing unique about that particular value.

It has been shown [25] that this state is dynamically stable except for a single neutral eigenvalue corresponding to a shift in $\alpha$.

In what follows, we consider a generalization of Equation 2.1, where we include some intrinsic quenched disorder:

$$\dot{\Delta}_j = \omega_j + \frac{K}{2N} \sum_{l=j-N}^{N} \sin(\Delta_l + \Delta_{j-l} - \Delta_j) \tag{2.4}$$

with the disorder constants $\omega_j$ drawn from a fixed, zero-mean distribution $g(\omega)$. We expect

such imperfections on physical grounds. In the optical resonator context, the $\omega_j$ arise from cavity imperfections and/or high-order dispersion effects.

### 2.3 Synchronization Behavior

We now consider the collective behavior of the ternary phase model, in particular the tendency to evolve into ordered states. Our approach is inspired by what is known about the Kuramoto model. To begin, we note that in the case of zero disorder ($\omega_j = 0$), Equation 2.4 is a gradient system $\dot{\Delta}_j = -\partial V/\partial \Delta_j$ with potential given by

$$V = -\frac{K}{6N} \sum_{j=1}^{N} \sum_{l=j-N}^{N} \cos(\Delta_l + \Delta_{j-l} - \Delta_j). \tag{2.5}$$

This structure implies the existence of locally stable perfectly synchronized states [28]. Extensive numerical simulations suggest that, for almost all initial conditions, the disorder-free system evolves to a perfectly synchronized state. (In simulations of Equation 2.1, a state satisfying the condition in Equation 2.2 may not be immediately obvious, owing to the angular nature of the variables. A simple check can be performed by plotting the difference of adjacent $\Delta_j$ *modulo* $2\pi$.) In view of this, we expect the dynamics of Equation 2.4 to exhibit a competition between the synchronizing influence of the coupling and the de-synchronizing influence of the disorder. The central issue is whether, and under what circumstances, the system exhibits an order-disorder transition, and if so what is the nature of the transition(s).

In order to investigate this question quantitatively, we introduce the following set of complex order parameters:

$$Z_j = \frac{1}{2N + 1 - j} \sum_{l=j-N}^{N} \mathrm{e}^{\mathrm{i}(\Delta_l + \Delta_{j-l})}. \tag{2.6}$$

$j = 1, 2, \ldots, N$. At steady state, $|Z_j|$ is observed to be independent of index $j$, up to

fluctuations of order $N^{-1/2}$. For a perfectly synchronized state Equation 2.2, $|Z_j|$ is exactly one, while for randomly distributed $\Delta_j$ it tends to zero. In practice, it is useful to average $|Z_j|$ over all oscillators and consider $\overline{|Z|}$ to be the overall order parameter.

Our simulations show that, for long times, trajectories of Equation 2.4 evolve linearly in time for all $\Delta_j$, *i.e.*

$$\Delta_j \to \alpha \cdot j + \delta_j + \Omega_j \cdot t. \tag{2.7}$$

The $\delta_j$ reflect deviation from Equation 2.2 due to the added disorder. From Equation 2.4, this relationship can only be satisfied if

$$\Omega_j = \Omega \cdot j. \tag{2.8}$$

Taking a weighted sum of the $N$ equations yields, since the coupling terms cancel,

$$\sum_{j=1}^{N} \dot{\Delta}_j \cdot j = \sum_{j=1}^{N} \omega_j \cdot j \tag{2.9}$$

so that

$$\sum_{j=1}^{N} (\Omega \cdot j) \cdot j = \sum_{j=1}^{N} \omega_j \cdot j \tag{2.10}$$

and so

$$\Omega = \frac{6}{N(N+1)(2N+1)} \cdot \sum_{j=1}^{N} \omega_j \cdot j. \tag{2.11}$$

For convenience, we can consider the co-rotating variables

$$\Delta'_j = \Delta_j - \Omega \cdot j \cdot t. \tag{2.12}$$

From Equation 2.7 and Equation 2.8, we can easily see that the transformed system $\Delta'_j$ evolves to a stationary state. Incidentally, this transformation also ensures the existence of

a constant of motion

$$\Gamma = \sum_{j=1}^{N} \Delta'_j \cdot j. \tag{2.13}$$

Unless otherwise noted, the simulations described below are performed in this frame by generating a set of $\omega_j$, calculating $\Omega$, and subtracting according to Equation 2.12.

To investigate order-disorder transitions in our system, we performed simulations using three different distributions for the $\omega_j$: uniform random, Gaussian random, and a systematic deterministic disorder to be described later.

The simulations were carried out as follows. We started by generating a random set of $\omega_j$ with unit variance. Multiplying this set by a factor $\sigma$ gives a standard deviation $\sigma$ while retaining comparable statistical properties. Starting with $\sigma = 0$ and random initial conditions, we numerically integrated Equation 2.4 until the system reached its stationary synchronized state. We then increased $\sigma$ by a small amount and continued integrating, until a new steady state was reached (identified by an unchanging averaged order parameter $\overline{|Z|}$). Iterating this process, the system eventually reaches the unsynchronized regime at $\sigma_1$. At some distance into the unsynchronized regime we reversed the process by gradually reducing $\sigma$. Eventually, at $\sigma_2$, the system begins to synchronize again.

Figure 2.1(a) and Figure 2.1(b) show typical results for random Gaussian and uniform disorder, respectively. The results are qualitatively similar. For small, increasing $\sigma$, the order parameter gradually decreases. At the critical value $\sigma_1$, there is a first-order transition beyond which the order parameter becomes negligible. Then, decreasing $\sigma$ induces another first-order transition at $\sigma_2$. The two transitions occur at different values of $\sigma$, resulting in a hysteresis loop. As expected, the fluctuations grow near the transition points.

This behavior is different than what one sees in the Kuramoto model. For comparison, results for the latter are shown in Figure 2.1(c) (Gaussian disorder) and Figure 2.1(d) (uniform disorder). For uniformly distributed disorder, the Kuramoto model shows a first-order transition with no hysteresis [29]. In the case of Gaussian distributed disorder, it shows a second-order transition.

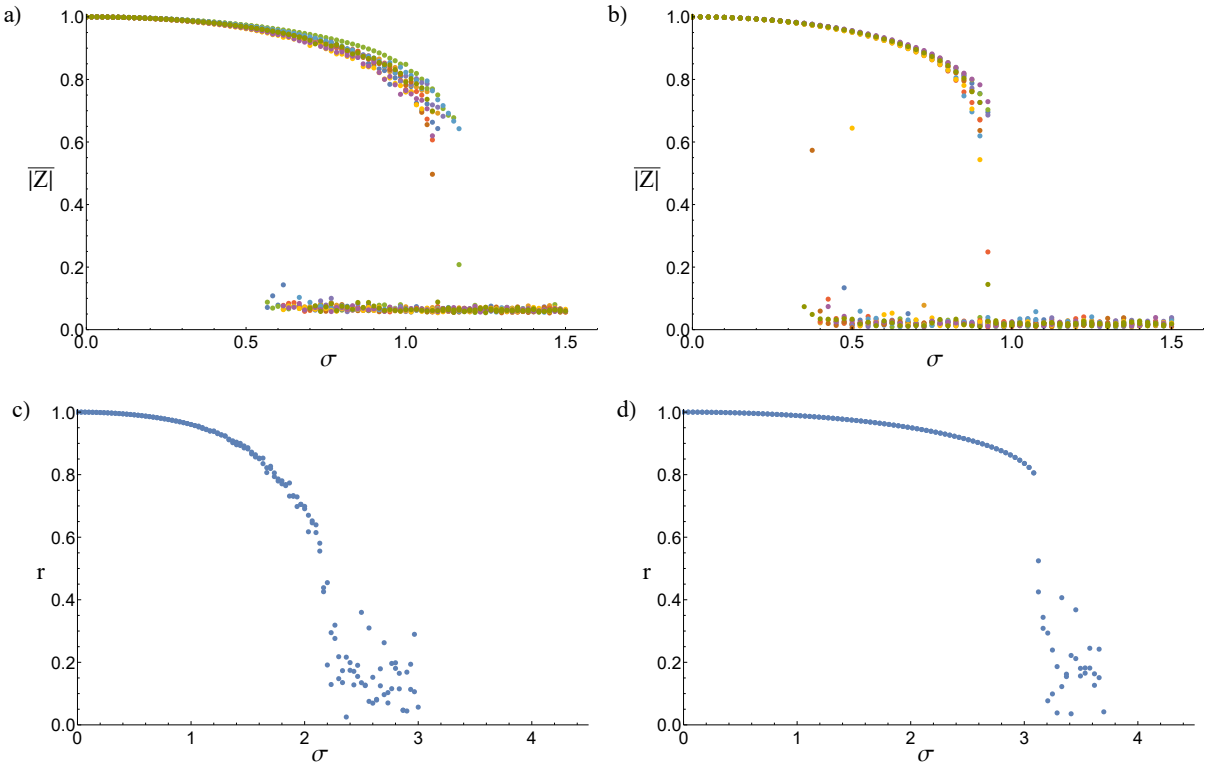


Figure 2.1: Order parameter versus standard deviation $\sigma$ of disorder distribution $g(\omega)$. (a) Ten realizations of Gaussian disorder in the ternary phase model for $N = 300$, $K = 4$. (b) Ten realizations of uniform disorder in the ternary phase model for $N = 300$, $K = 2$. (c) Gaussian disorder in the Kuramoto model for $N = 400$, $K = 4$. (d) Uniform disorder in the Kuramoto model for $N = 300$, $K = 4$.

In addition to random disorder, we also considered disorder of the form

$$\omega_j = \frac{c}{N^3} \cdot j^3 \tag{2.14}$$

with $c$ the effective "width" of the distribution. This choice is motivated by higher-order dispersion effects that arise in the micro-resonator problem [25, 23]. The behavior in this case can be understood heuristically as follows. As $c$ is increased, the oscillators with large $j$, i.e. those far from the pump mode, acquire an intrinsic frequency much larger than the coupling constant and thus become completely unlocked from the rest of the population. The lower $j$ oscillators still have relatively low disorder, and can synchronize. The result is that the population is synchronized up to a critical $j$ above which the oscillators are

effectively free-running. This is illustrated in Figure 2.2(a) by plotting $\dot{\Delta}_j$ and $\omega_j$ versus

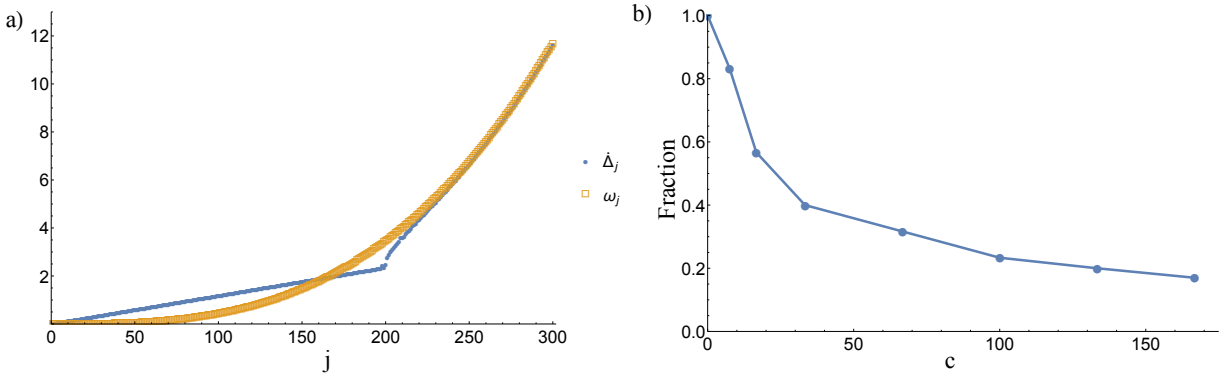


Figure 2.2: Cubic disorder in the ternary phase model. (a) $\dot{\Delta}_j$ and $\omega_j$ versus $j$ for the ternary phase model with cubic disorder at $c = 12$. (b) Fraction of locked oscillators versus width $c$ in the ternary phase model with cubic disorder.

$j$ in the non-co-rotating frame. The locked oscillators fall on a straight line reflecting the synchronization conditions in Equation 2.7 and Equation 2.8 while the unlocked oscillators, beginning at $j \approx 200$, rotate at their intrinsic frequencies. While the locked oscillators can be thought of as being frequency locked, this is really a result of their phase locking; for the ternary model the two are necessarily connected through the synchronization condition.

Carrying out simulations using the same protocol as before, we find that the fraction of locked oscillators (those with $\dot{\Delta}_j$ falling on the straight line) decreases continuously to zero with no observed transition or hysteresis (Figure 2.2(b)). This suggests that cubic dispersion merely dilutes the total synchronization; for random noise, the first-order transitions enforce a critical threshold above which no synchronization is possible.

## 2.4 Thermodynamic Limit

In order to move beyond simulations, we formulated a thermodynamic limit corresponding to an infinite number of oscillators on a lattice with uniform spatial density. We show that, in this limit, there are no fluctuations and the collective state can be uniquely identified.

Unlike the all-to-all coupling of oscillators in the Kuramoto model, the ternary coupling in Equation 2.4 is index-dependent. We therefore consider the oscillators to lie on a discrete

lattice corresponding to $j = 1, 2, \ldots, N$. Inspired by [30], we consider a spatial continuum of oscillators which can be described by an explicitly position-dependent probability density.

First, we note that the equation of motion Equation 2.4 can be written in terms of the order parameters Equation 2.6 as

$$\begin{aligned} \dot{\Delta}_j &= \omega_j + \frac{2N+1-j}{2N} K R_j \sin(\psi_j - \Delta_j), \\ Z_j &= R_j \mathrm{e}^{\mathrm{i}\psi_j}. \end{aligned} \tag{2.15}$$

In this form, the individual oscillators appear decoupled which allows for a self-consistent calculation of the order parameters. The order parameters $Z_j$ are written explicitly as

$$Z_j = \frac{1}{2N+1-j} \sum_{l=j-N}^{N} \mathrm{e}^{\mathrm{sgn}(l)\mathrm{i}\Delta_{|l|}} \mathrm{e}^{\mathrm{sgn}(j-l)\mathrm{i}\Delta_{|j-l|}} \tag{2.16}$$

reflecting the antisymmetry condition $\Delta_{-j} = -\Delta_j$. The $Z_j$ can be expressed in terms of a probability distribution rather than an explicit sum as

$$\begin{aligned} Z_j = \frac{1}{2N+1-j} \sum_{l=j-N}^{N} \int_0^{2\pi} \mathrm{d}\Delta \int_0^{2\pi} \mathrm{d}\Delta' \int_{-\infty}^{\infty} \mathrm{d}\omega \int_{-\infty}^{\infty} \mathrm{d}\omega' \\ \times P(\Delta, \Delta', \omega, \omega', |l|, |j-l|) \mathrm{e}^{\mathrm{sgn}(l)\mathrm{i}\Delta} \mathrm{e}^{\mathrm{sgn}(j-l)\mathrm{i}\Delta'} \end{aligned} \tag{2.17}$$

where $P(\Delta, \Delta', \omega, \omega', x, x')$ is the joint probability density of the oscillator at $x$ having phase $\Delta$ and disorder $\omega$ while the oscillator at $x'$ has phase $\Delta'$ and disorder $\omega'$. In the spirit of Equation 2.15, we consider the oscillators to be independent so that the probability density $P$ can be approximated as

$$P(\Delta, \Delta', \omega, \omega', |l|, |j-l|) = \rho(\Delta, \omega, |l|) \rho(\Delta', \omega', |j-l|) \tag{2.18}$$

with $\rho$ the probability density for a single oscillator parameterized by position.

Because the coupling depends on oscillators at two different positions, the density $\rho$ appears twice. This is one of the major structural novelties of the model and significantly complicates stability analysis of the unsynchronized state.

In order to treat the infinite oscillator limit, in which case the probability densities vary continuously in space, we introduce a spatial coordinate $x$ such that

$$\begin{aligned} x &= \frac{j-1}{N-1}, \\ 0 &\leq x \leq 1. \end{aligned} \tag{2.19}$$

From (Equation 2.19), $\mathrm{d}j = (N-1)\mathrm{d}x$, and the summation over $l$ transforms according to

$$\frac{1}{2N+1-j} \sum_{l=j-N}^{N} \mathrm{d}j = \frac{N-1}{2N-(N-1)x} \sum_{y=\frac{(N-1)x-N}{N-1}}^{1} \mathrm{d}y. \tag{2.20}$$

Taking $N \to \infty$, the sum becomes an integral and position $x$ becomes continuous, leading to

$$\begin{aligned} Z(x) = \frac{1}{2-x} \int_{x-1}^{1} \mathrm{d}y \int_{0}^{2\pi} \mathrm{d}\Delta \int_{0}^{2\pi} \mathrm{d}\Delta' \int_{-\infty}^{\infty} \mathrm{d}\omega \int_{-\infty}^{\infty} \mathrm{d}\omega' \\ \times \rho(\Delta, \omega, |y|)\rho(\Delta', \omega', |x-y|)\mathrm{e}^{\mathrm{sgn}(y)\mathrm{i}\Delta}\mathrm{e}^{\mathrm{sgn}(x-y)\mathrm{i}\Delta'}. \end{aligned} \tag{2.21}$$

The full thermodynamic system, completely described by $\rho$, is governed by the continuity equation

$$\begin{aligned} \frac{\partial \rho}{\partial t} + \frac{\partial}{\partial \Delta}\left(\rho \dot{\Delta}\right) = 0, \\ \dot{\Delta} = \omega + (1 - x/2)KR(x)\sin(\psi(x) - \Delta), \\ Z(x) = R(x)\mathrm{e}^{\mathrm{i}\psi(x)} \end{aligned} \tag{2.22}$$

and the constraints

$$\int_0^{2\pi} \mathrm{d}\Delta \int_{-\infty}^{\infty} \mathrm{d}\omega \rho(\Delta, \omega, x) = 1,$$
$$\int_0^{2\pi} \mathrm{d}\Delta \rho(\Delta, \omega, x) = g(\omega) \tag{2.23}$$

where $g(\omega)$ is the probability density for each oscillator's disorder.

Having established the evolution equations for the thermodynamic limit, we may calculate the order parameter $R = \overline{|Z|}$ as a functional of the disorder distribution $g(\omega)$. The details of the calculation are relegated to Appendix A, but the final result is

$$R = \int_0^1 \mathrm{d}y \left[ \frac{(2-y)KR}{2} \int_{-\frac{\pi}{2}}^{\frac{\pi}{2}} \mathrm{d}\theta \; g\left[ \frac{(2-y)KR}{2} \sin\theta \right] \cos^2\theta \right]^2, \tag{2.24}$$

valid for even, unimodal $g(\omega)$.

One sees immediately that $R = 0$ is always a solution. To find non-zero solutions, Equation 2.24 can be numerically solved for any given $g(\omega)$. The resulting predictions for Gaussian and uniform disorder are shown in Figure 2.3 alongside values from direct

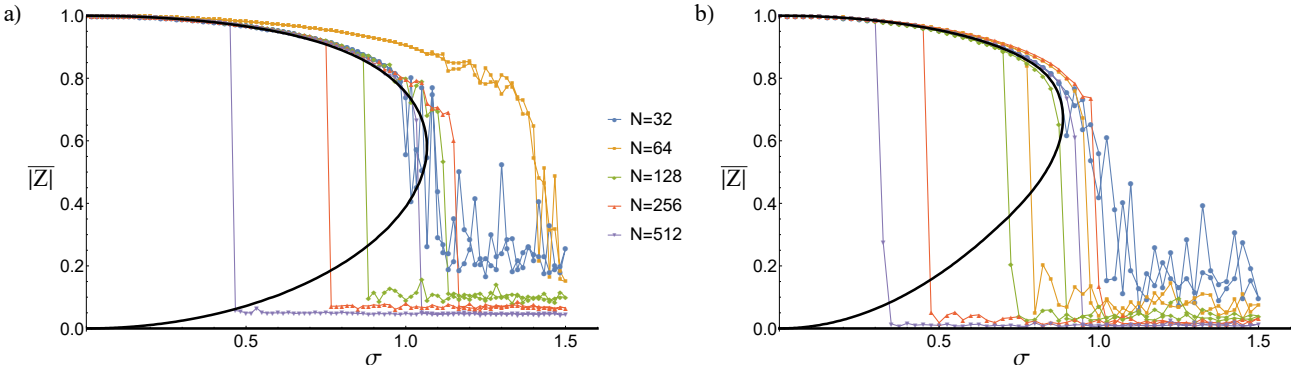


Figure 2.3: Predicted order parameter in the infinite oscillator limit (thick line) for (a) Gaussian disorder, (b) uniform disorder. Agreement improves with a larger number of oscillators $N$.

simulation for different $N$. As $N$ is increased, agreement along the upper branch improves

considerably. Since $|Z|$ is non-negative, convergence along the lower incoherent branch is much slower. The middle solution branch is presumably unstable, as is the case for a saturating subcritical pitchfork bifurcation [31].

Curiously, the unsynchronized state is stable for a wider range of $\sigma$ as $N$ is increased, and may even be stable for all values as $N \to \infty$. This would be consistent with the theoretically predicted curve in which the middle branch and $R = 0$ branch meet exactly at the origin. Bistability of the synchronized and unsynchronized states would have important implications for the micro-resonator problem since even a perfect device could fail to achieve mode locking.

While our previous analysis hasn't addressed stability, we note that linear stability of even the trivial $R = 0$ state is complicated by the fact that the order parameter is quadratic in $\rho$. This can be understood from the following argument without a complete stability calculation. The incoherent $R = 0$ state is represented by the uniform density

$$\rho_0 = \frac{g(\omega)}{2\pi}. \tag{2.25}$$

Evaluation of the order parameter Equation 2.21 using a perturbed solution of the form $\rho_0 + \epsilon\delta\rho$ yields zero to linear order in $\epsilon$; one of the two factors of $\rho$ must be $\rho_0$, causing its associated exponential in $\Delta$ to vanish upon integration. However, the order parameter is responsible for coupling the oscillators as shown in Equation 2.22. When it vanishes, $K$ disappears from the equations and so cannot be responsible for a bifurcation. As a result, a nonlinear stability analysis is required to describe any synchronizing transition from the incoherent state.

## 2.5 Conclusions and Open Questions

In this Chapter, we investigated the synchronization behavior of a new phase model. We found that its transitions are characteristically different from those found in the classic

Kuramoto model. We developed a thermodynamic, continuum limit which we used to calculate the order parameter for different disorder distributions. Although the predicted values for the order parameter agree well with simulations, the onset of instability for the unsynchronized solution is currently unexplained. With the enormous utility of the Ott-Antonsen ansatz [32] for the continuum limit of the Kuramoto model, it is natural to wonder if a similar dimensional reduction can be performed for the ternary model.

In addition to its novel dynamical properties, investigating the ternary phase model provides insight into the robustness of the synchronization process in optical microresonator cavities. However, the ternary phase model only approximates the dynamics of the original LLE. In particular, the amplitudes of all Fourier modes are assumed to be stationary. While this is a standard assumption in phase reduction theory, amplitude dynamics could account for additional behavior relevant to the formation of stable pulsation. Other effects such as finite-size fluctuations and the inclusion of non-identical coupling constants $K_j$ could also be explored. The latter has been investigated in the absence of disorder [25].

Perhaps the greatest outstanding challenge in studying the ternary phase model is the issue of stability. The difficulty of even linear stability analysis for the Kuramoto model is well known [33]. For the ternary model, linear analysis fails and a strictly nonlinear approach is apparently needed.

# CHAPTER 3

# TERMINATING SPIRAL WAVES WITH A SINGLE DESIGNED STIMULUS: TELEPORTATION AS THE MECHANISM FOR DEFIBRILLATION

## 3.1 Introduction.

Spiral waves have been shown to exist in many chemical [34] and biological [35, 36] systems, with many of these supporting spiral-wave-mediated turbulence [37]. Of particular clinical significance are the spiral waves of electrical activity that underlie tachycardia and fibrillation in the heart [12, 13]. Even before spiral waves were recognized as drivers of tachycardia and fibrillation in the 1990s [38], termination of these deadly arrhythmias was shown possible by large electric shocks as early as 1899. However, it was not until 1947 that defibrillation was shown to be successful in the clinic [39]. Despite the advent of clinical treatment, the mechanisms responsible for successful defibrillation are still not fully understood [40]. Limited experimental mapping of cardiac activity during fibrillation and shock-based treatment has led to a number of ambiguously compatible theories [41]. A particularly compelling aspect of the puzzle is that defibrillating shocks can actually initiate or reinitiate fibrillation if applied during certain vulnerable time periods or when localized to certain vulnerable locations. In this Chapter, a topological framework for characterizing cardiac activation is presented which unifies seemingly disparate mechanisms of defibrillation. In particular, this framework elucidates how reentrant spiral rotors are initiated and eliminated by localized stimulus. This insight provides a deeper understanding of the general mechanism behind defibrillation and accordingly informs the development of more efficient and lower energy defibrillation therapies.

Defibrillation usually requires electric shocks on the order of 5-7 Joules for internal and 200-300 Joules for external application [42]. These high-energy shocks are very painful

and can damage heart tissue but are required to prevent initiation of new spiral waves [43]. While currently there are no clinically viable low-energy defibrillation strategies, several new methods have been developed and tested computationally and experimentally. One consists of a multi-stage series of low-energy pulses intended to subsequently unpin and remove reentrant spiral waves [44]. Another example is the low-energy antifibrillation pacing (LEAP) method [45], which uses a series of fast pulses at a frequency close to the dominant frequency of arrhythmia to eliminate spiral waves. Both of these methods utilize the mechanism of virtual electrodes—tissue activation driven by the heart's natural heterogeneities [43, 42]. Other studies have used concepts from nonlinear dynamics to determine optimal defibrillation stimulus timing and strength by calculating phase [46] and isostable [47] resetting curves. However, neither of these methods directly address the topological spatiotemporal coupling responsible for spiral waves and both require detailed spatial information of the system state. In this Chapter, we demonstrate how a single minimal stimulus can be designed from topological considerations to automatically eliminate reentrant spiral wave singularities in a complex fibrillating state.

### 3.2 Defining level set contours and phase singularities.

In order to characterize the complex spatiotemporal dynamics of an excitable system, regions in space are designated locally excited, refractory, or recovered. For a multi-component system $\vec{u}(\vec{x}, t)$, indicator functions $f(\vec{u})$ and $g(\vec{u})$ are defined such that regions where $f > 0$ are excited and regions where $g > 0$ are refractory [48]. The level sets $f = 0$ and $g = 0$ then define one-dimensional contours marking the boundaries of excited and refractory regions, respectively. Excited or refractory fronts can be differentiated from backs on a given zero-level set by the sign of the opposite indicator function [48, 49]. This results in a set of four distinct contours as defined in Table 3.1.

For two-variable reaction-diffusion systems such as the FitzHugh-Nagumo (FHN) [50]

Table 3.1: Definitions and plotting conventions for the four topological level set contours.

| | | |
|---|---|---|
| Excited front | $f = 0, g < 0$ | Denoted by solid black line |
| Refractory front | $g = 0, f > 0$ | Denoted by solid white line |
| Excited back | $f = 0, g > 0$ | Denoted by broken black line |
| Refractory back | $g = 0, f < 0$ | Denoted by broken white line |

and Karma [51] models, $\vec{u} = \{u, v\}$ and obeys

$$\begin{aligned} \frac{\partial u}{\partial t} &= h(u, v) + D\nabla^2 u \\ \frac{\partial v}{\partial t} &= w(u, v). \end{aligned} \tag{3.1}$$

In this case, the indicator functions $f$ and $g$ can simply be taken to be

$$f = u - u_{\text{th}}, \qquad g = v - v_{\text{th}} \tag{3.2}$$

for some threshold values $u_{\text{th}}, v_{\text{th}}$. Other common choices of $f$ and $g$ include the system variables' time derivatives [48] or time-delayed values [52], local curvature [53], and normal velocity [54]. Each choice is topologically equivalent and gives comparable results [48, 52]. Gurevich et al. have shown how to construct valid combinations using only noisy voltage data in both simulation and experiment [55, 56]. In their implementations, $f$ and $g$ are determined by the extrema and inflection points of the local voltage and do not require measurement of the underlying gating currents. Figure 3.1 shows the level set contours using Equation 3.2 for a rightward-traveling pulse in the FHN model on a 2D domain (see Appendix B for models and parameters). Such a pulse displays how local excitation must pass through excited front, refractory front, excited back, and refractory back in sequence before returning to rest.

One of the most important uses of level set contours is the identification of spiral wave tips. These are isolated points at the center of spiral waves where wavefront and wave-back intersect to form a continuous source of reentrant excitation. Spiral tips are mostly

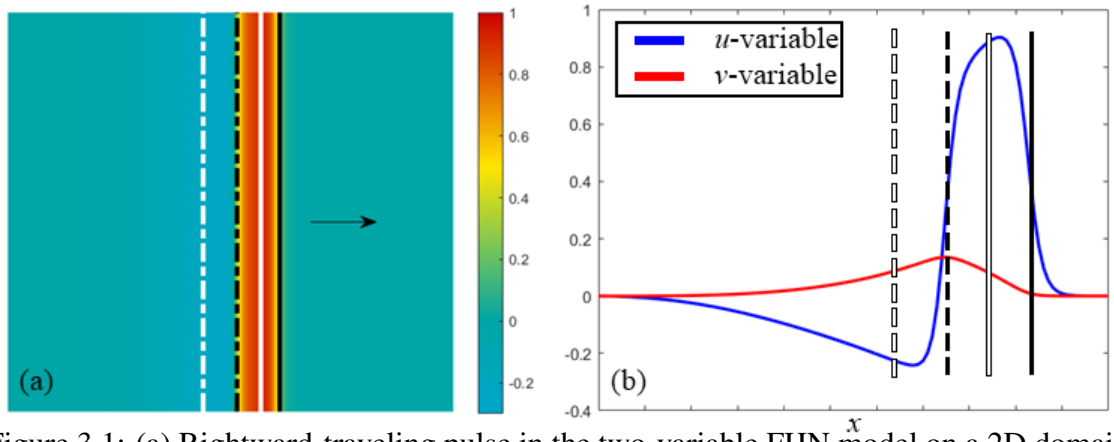


Figure 3.1: (a) Rightward-traveling pulse in the two-variable FHN model on a 2D domain. Excited and refractory contours are superimposed following the conventions in Table 3.1. (b) One-dimensional cross section of (a) showing both the $u$ (blue) and $v$ (red) variables. Level set contours are overlaid at positions from (a).

commonly described as phase singularities in a complex order parameter given by

$$Z(\vec{u}) = r\mathrm{e}^{\mathrm{i}\theta} = f(\vec{u}) + g(\vec{u})\mathrm{i}. \tag{3.3}$$

in analogy with homotopy theories used in condensed matter physics [57]. The spatial line integral of the phase $\theta$ around a phase singularity (known as the topological charge) is equal to $\pm 1$ with the sign determining the corresponding spiral's chirality [52]. Equivalently, the amplitude $r$ vanishes exactly on a phase singularity, that is, when $f = g = 0$ and the level set contours of Table 3.1 intersect. From Equation 3.2, this implies that $u = u_{\text{th}}, v = v_{\text{th}}$ at the singularity. The chirality can be obtained from the level sets by calculating the sign of $\hat{z} \cdot (\nabla f \times \nabla g)$ at the singularity.

The framed region in Figure 3.2(a) shows the contours and phase singularity for a single spiral wave in the FHN model. Figure 3.2(b) shows the same spiral but in the phase space of the $f$ and $g$ indicator functions. The periodic behavior of spiral rotation manifests as a dense collection of points forming a closed loop. Because the origin is interior to this loop, the order parameter acquires a singularity in the presence of a spiral wave.

The topological properties of phase singularities have long been understood to play a major role in the initiation and persistence of spiral-wave-mediated turbulence respon-

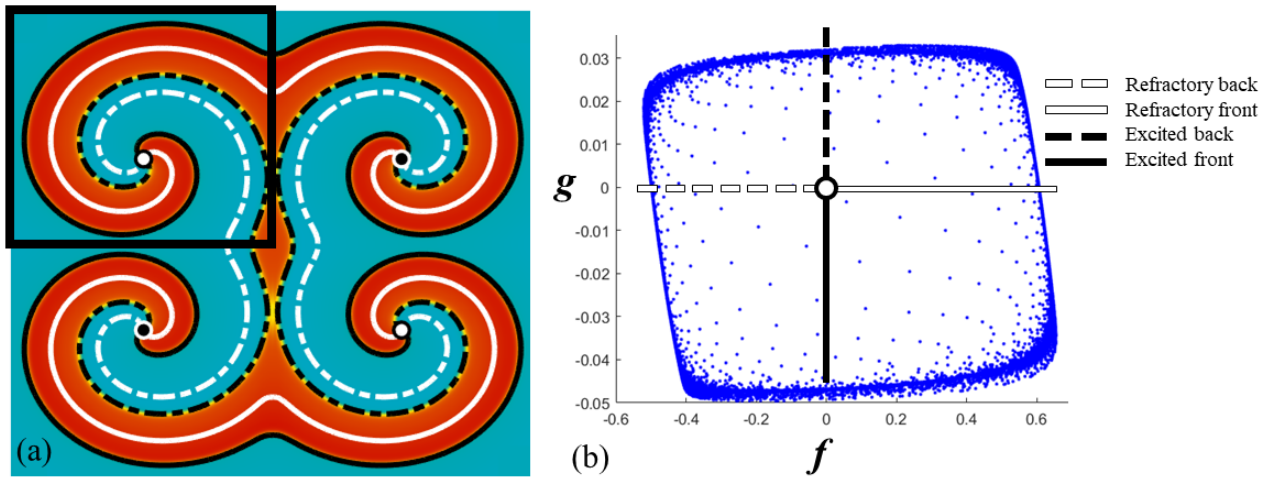


Figure 3.2: (a) Single spiral wave in the two-variable FHN model on a 2D domain with reflective boundary conditions (dark frame). The extended domain shows how mirrored spiral waves allow for conservation of topological charge. Chirality is indicated with white (black) circles for counterclockwise (clockwise) spiral tips. (b) Phase space representation of the spiral wave shown in (a). Blue dots show the $f - g$ phase space position at every point in the physical 2D domain. Level sets are shown using conventions in Table 3.1.

sible for cardiac arrhythmias [12]. Winfree used topological arguments about the phase of the complex order parameter to show how singularities can be created or destroyed by particular stimuli [11, 9]. A significant result is that (excluding boundary interactions), singularities can only be created or destroyed in pairs of opposite chirality. This principle is commonly referred to as conservation of topological charge and follows simply from the continuity of $\vec{u}$ and the indicator functions $f, g$ [48, 9, 58, 59]. Additionally, every singularity is uniquely connected to a singularity of opposite chirality by each of the four contours.

Topological charge is not conserved on domains with zero flux (or reflective) boundary conditions, which are commonly used in cardiac simulations [60]. However, if the domain is mirrored as in Figure 3.2(a), the extended domain does conserve topological charge. In this construction spirals with contours terminating at boundaries are connected to a mirrored spiral with opposite chirality. It follows that in order to eliminate spiral wave turbulence (or fibrillation), it is necessary to annihilate every singularity by merging it with a singularity of opposite chirality inside the domain or with its mirror image at a domain

boundary. In the next section we show how this can be accomplished with an excitatory stimulus using the topological structure of the level set contours.

### 3.3 Terminating singularities with a single designed stimulus.

While phase and level set descriptions are topologically equivalent and are explicitly related through Equation 3.3, each is suited to different systems. In oscillatory media, phase has a natural definition in terms of the underlying limit cycle and is thus the natural object to study [1]. The excitable-refractory paradigm of excitable media, however, is better represented by the level set contours. In particular, they can be used to understand how stimulus leads to the creation or annihilation of spiral wave singularities.

A classic procedure for initiating a pair of spiral wave singularities via excitatory stimulus is the S1-S2 protocol [61, 62]. First, a stimulus S1 is applied to generate a traveling pulse. A second localized stimulus S2 is then applied behind the pulse. The excited wavefront of S2 intersects with the refractory back of the S1 pulse and generates a pair of singularities that develop into spiral waves as illustrated in Figure 3.3. Because the simulation uses zero flux boundary conditions, a stimulus S2' localized near the boundary may produce a single spiral singularity and violate conservation of topological charge.

Winfree originally explained the S1-S2 generation of singularities in terms of the continuous gradient of phase produced in the complex order parameter [11]. For excitable media, however, the contours tell a simpler story. By definition, the refractory back contour separates regions which will respond to stimulus by exciting from regions which will be unexcited. This provides a mechanism for creating unidirectional propagation, as excitation can only travel away from the refractory region—left in the case of Figure 3.3(b). From Figure 3.1, we know that the excited portion of a traveling pulse contains an excited front, refractory front, and excited back. Stimulating a refractory back contour thus replaces it with this sequence of three contours. However, since the stimulus is localized, only a finite segment of the refractory back contour is replaced. At the boundary of the stimulus, the re-

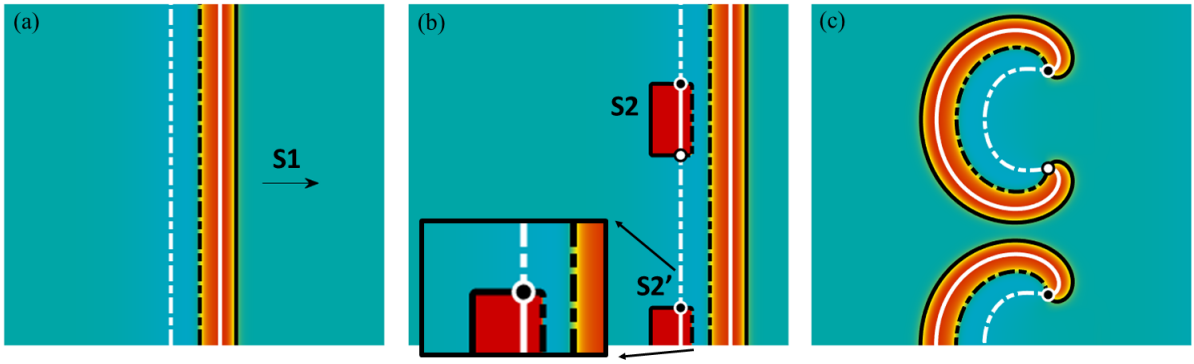


Figure 3.3: Creating spiral waves with the S1-S2 protocol. (a) A rightward-traveling pulse generated by exciting the left boundary with stimulus S1. (b) An opposite pair and an isolated singularity are created by applying localized S2 and S2' stimuli to the refractory back of the S1 pulse. As shown in the inset, the singularities are generated at the convergence of all four level set contours. (c) The singularities persist and form stable spiral waves that act as continuous sources of excitation.

fractory back contour must connect with this sequence and therefore produce a singularity. This is illustrated in the inset of Figure 3.3(b).

While the S1-S2 protocol illustrates clearly how singularities can be created, it is not immediately obvious how to reverse this procedure in order to eliminate them. Consider the new stimuli shown in Figure 3.4(a) superimposed on the configuration from Figure 3.3(c). These stimuli cover the clockwise singularities and a significant portion of their refractory back contours. The result of the stimuli, shown in Figure 3.4(b), is that the singularities are "teleported" along the contour to the end of the stimulus. This brings the paired spiral very close to its partner and the isolated spiral very close to its mirrored image at the boundary. The nearby pairs then mutually annihilate due to their proximity. If the stimulus is allowed to cover the entire refractory back, the existing singularities will be teleported together and eliminated instantaneously as in Figure 3.4(c). This whole process can be understood from the contour topology in the same way as the S1-S2 protocol. Stimulating the refractory back once again replaces it with the excited front, refractory front, excited back contour sequence. This time, however, it causes the contours to disconnect (Figure 3.4(c)), thereby removing the singularities at either end of the contour.

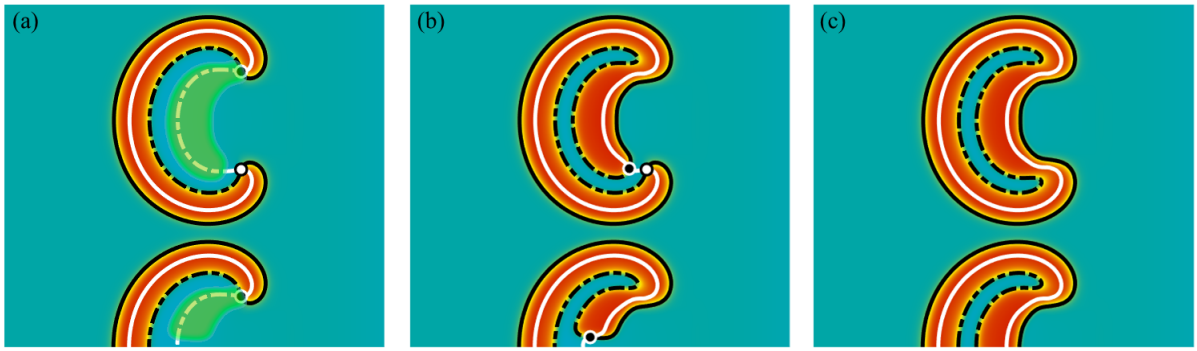


Figure 3.4: Terminating spiral waves with a single stimulus. (a) Regions covering the refractory back contours are selected for stimulus (light green). (b) Applying the stimulus "teleports" the existing clockwise singularities along the refractory contours toward their counterparts. (c) The opposite pairs of singularities mutually annihilate and the contours reform without intersection.

Because every singularity is connected to a singularity of opposite chirality, a single stimulus targeting the refractory back can always be designed to teleport and eliminate all internally paired and boundary paired singularities. Moreover, excitation of the full refractory back contour can be taken as the necessary and sufficient condition for total defibrillation; the only way to remove singularities is to modify their topology in this manner. It should also be noted that the same topological arguments allow defibrillation using instead *de*exciting stimuli targeting the refractory *front*; both possibilities were discussed by Keener in [49].

Previous theoretical analyses have reported a defibrillation threshold for domain-wide stimulation [40, 63]. In that case, even refractory regions of tissue must be excited such that propagating fronts only contract and dissipate [64]. In our proposed method, only a fraction of the domain needs stimulation. Additionally, since only the recovered region (which is readily excitable) of the refractory back needs to be excited, the stimulation strength can be well below the defibrillation threshold.

In practice, the defibrillating stimulus is constructed by applying a current $I_{\text{stim}}$ to the voltage variable $u$ wherever $f < 0$ and $|g| < g_{\text{th}}$. The zero threshold $g_{\text{th}}$ gives the stimulus a finite thickness about the refractory back contour. If $I_{\text{stim}}$ or $g_{\text{th}}$ are too small, the stimulus

will fail to permanently remove every singularity; although they may disappear initially, pairs of singularities can spontaneously reform and persist.

Figure 3.5 and Figure 3.6 show how the designed stimuli successfully teleport and remove all singularities in complex, multi-spiral states regardless of whether singularities are internally paired or connected to the domain boundary. Some configurations contain refractory backs not connected to singularities (e.g. upper left corner in Figure 3.5(a)). Stimulation of these contours is not required for defibrillation and is omitted in Figure 3.6. Connections between pairs of singularities can also switch over time. Figure 3.5(d) shows an alternate configuration obtained a quarter of rotation after Figure 3.5(a) in which the two lower spirals have become connected. Defibrillation is successful in both models (FHN and Karma) despite the stimuli covering less than 10% of the domain in the latter case.

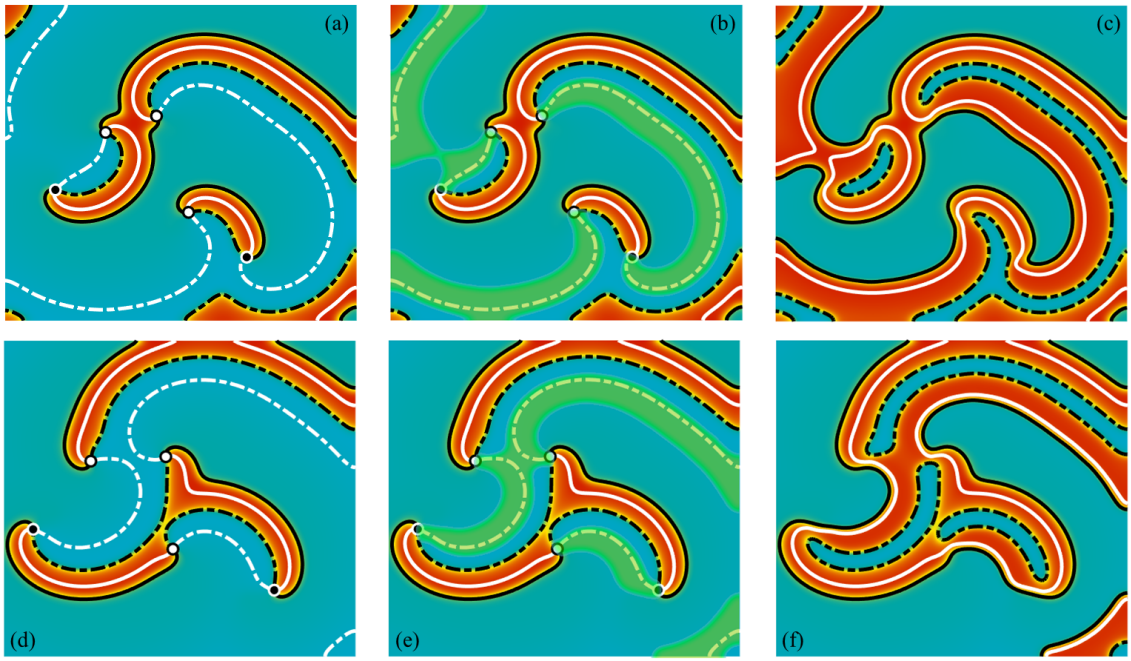


Figure 3.5: (a) A complex multi-spiral state in the FHN model. (b) Stimulus pattern designed to teleport all pairs of singularities along their refractory contours. (c) Successful defibrillation immediately after stimulus. (d) The complex state from (a) evolved in time such that the two lower spirals are connected. (e) Altered stimulus pattern for the configuration in (d). (f) Successful defibrillation of (d).

Teleportation can also unpin spiral waves bound to an obstacle. Figure 3.7 shows this

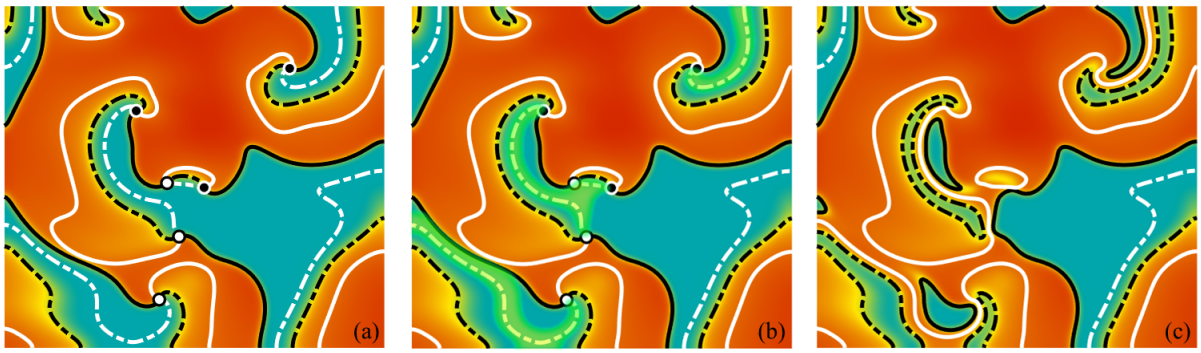


Figure 3.6: (a) Fibrillating spiral breakup in the Karma model. (b) Stimulus pattern designed to teleport all pairs of singularities along their refractory contours. (c) Successful defibrillation immediately after stimulus.

process for a single spiral in the FHN model. A stimulus along the refractory back instantaneously teleports the singularity off the obstacle (Figure 3.7(b) and (c)). However, the stimulus along the obstacle generates a new pair of singularities a short time later (Figure 3.7(d)). These singularities rotate around the obstacle until they meet and annihilate on the opposite side (Figure 3.7(d) and (e)). The spiral is then unpinned (Figure 3.7(f)), but will continue to generate new spiral pairs at the obstacle whenever the spiral arm meets it. If the teleporting stimulus extends along the entire contour, the original spiral will be both unpinned and annihilated as it is teleported to the boundary.

To demonstrate the generality of designing stimuli to defibrillate by teleportation, we have successfully applied it using more physiologically accurate cardiac cell models including the 8-variable Beeler-Reuter model [65], the 19-variable TNNP model [66], and the 41-variable OVVR model [67]. Although the phase space of these models is complicated by their large number of dimensions, suitable indicator functions can still be constructed to properly characterize the level set contour topology [48]. We find both the $f$ (inactivation calcium) and $h$ (inactivation sodium) gate variables functional substitutions for the generic gate variable in Equation 3.2 while suitable thresholds are identified by inspecting the phase-space portrait as in Figure 3.2(b). Real-time interactive WebGL programs [68] for generating defibrillating stimuli in these models are provided at the author's website

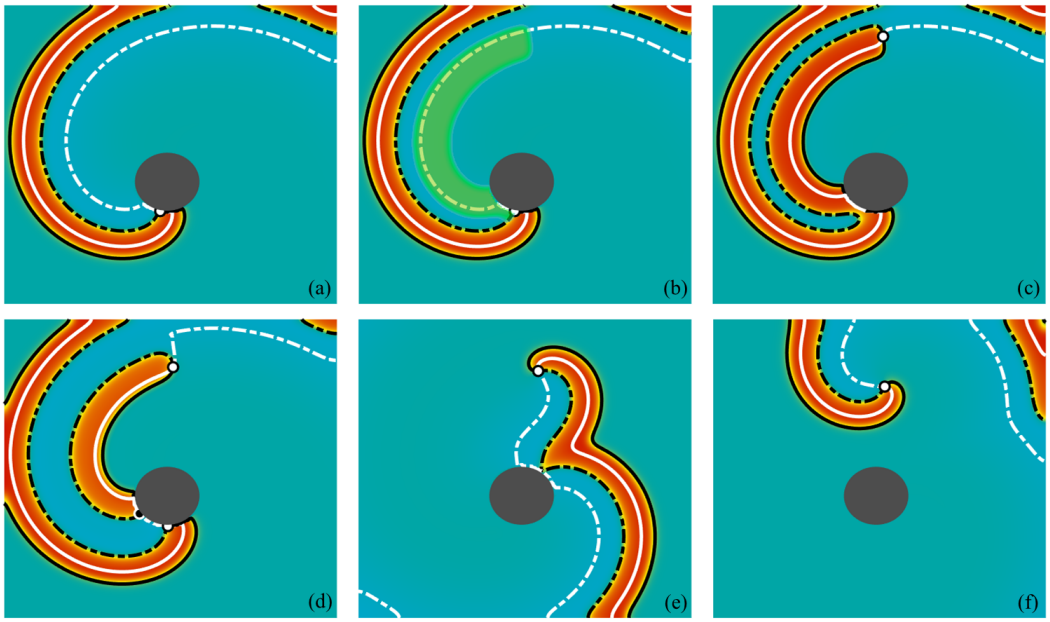


Figure 3.7: (a) A single spiral wave pinned to an obstacle in the FHN model. (b) Stimulus pattern designed to teleport the spiral away from the obstacle. (c) Immediate result of stimulation. The spiral singularity is instantaneously teleported to the edge of the stimulus. (d) Excitation at the obstacles creates a new pair of singularities. (e) The new singularity pair meets and annihilates on the opposite side of the obstacle. (f) The original spiral wave is completely unpinned.

[69].

In simulations, defibrillation by teleportation is made easier by the single-pixel resolution of the exciting stimulus. In order to emulate an experimentally realistic setup, we implemented an array of circular electrodes where stimulus may be applied. Figure 3.8(a) shows an example stimulus pattern for an isolated spiral wave in the FHN model. The domain was divided into a $9 \times 9$ grid. If $f < 0$ and $|g| < g_{\text{th}}$ were satisfied within a grid cell, a circular stimulus was applied to the center. Because of the pulses' discontinuity, many new pairs of singularities are created via the S1-S2 mechanism as shown in Figure 3.8(b). However, as they are very close, the pairs then spontaneously annihilate to produce the continuous excited back shown in Figure 3.8(c). The original singularity is then effectively teleported to the boundary and defibrillation is successful. If the electrodes are insufficiently dense, however, newly created pairs may persist indefinitely and actually increase

the total number of singularities.

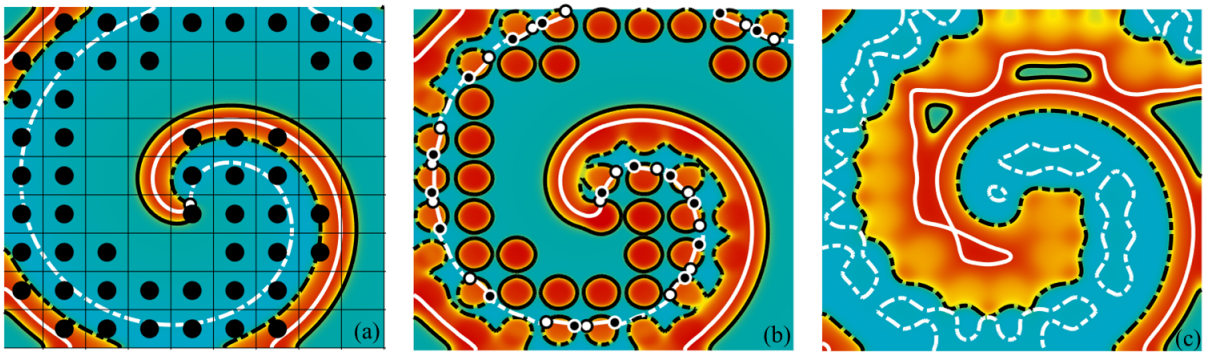


Figure 3.8: Defibrillation by teleportation using an equally-spaced electrode array. (a) Stimulus pattern generated by electrodes (black) firing for $f < 0$ and $|g| < g_{\text{th}}$ in each grid cell. (b) Immediate result of stimulation. Many transient singularities form via the S1-S2 mechanism. (c) Nearby singularities spontaneously annihilate and the original singularity is teleported to the boundary.

### 3.4 Teleportation as the mechanism for defibrillation.

While direct application of a designed stimulus may not be currently possible in the clinic, sufficient activation of the refractory back is nevertheless necessary for successful defibrillation regardless of the activation source. The shock-induced teleportation of spiral wave singularities thus serves as a mechanistic explanation for defibrillation in real tissue at both high [40, 70] and low energies [44, 42]. During high-energy shocks, enough virtual electrodes (VE) are activated to excite the entire heart and thus stimulate continuously along the refractory backs connecting reentrant spiral waves. Pairs of spirals are instantly teleported together, while isolated spirals are teleported to domain boundaries. Low-energy shocks in general do not excite everywhere [42], but if enough of the refractory back is stimulated, spirals are teleported close enough together to spontaneously annihilate.

Under the theory presented here, two effects can contribute to the failure of high- and low-energy shocks to successfully defibrillate. First, spirals can fail to be teleported close enough to annihilate if their refractory backs are insufficiently stimulated by VE excitation. This may occur during high-energy defibrillation if at least one reentrant pair is not

fully teleported together, resulting in persistent rotors which then reinitiate fibrillation [70]. Second, virtual electrodes may discontinuously stimulate refractory backs resulting in the initiation of new rotors as in the S1-S2 mechanism [43, 42]. This explains the failure of low-energy defibrillation [70, 71]. While a single low-energy shock may fail to completely defibrillate, multi-shock therapies such as LEAP may succeed by annihilating more pairs by teleportation each shock than are created via S1-S2 initiation [45].

### 3.5 Conclusions and Open Questions

By considering the level set contours organizing excitable dynamics, we have demonstrated a novel minimal defibrillation strategy capable of automatically eliminating any phase singularities responsible for spiral wave turbulence. Using a designed stimulus, pairs of connected spiral wave tips are instantaneously moved close together by a mechanism we dub teleportation such that the tips attract and mutually annihilate. The topological nature of this method makes it model-independent and applicable to experiment. A particularly promising experimental testbed would be optogenetically modified cardiac monolayers [72, 73]. Previous studies have shown how rotors in this system may be eliminated using heuristically chosen regions of activation [72]. Spatially resolved optical control combined with established methods for determining contours in experiment [55, 56] would allow for exact replication of our computational examples and provide a systematic method of eliminating rotors. Although time delays between mapping and stimulus design are unavoidable, wave velocities in cardiac monolayers are on the order of 20cm/s. Modern GPU calculations for analyzing the contours can easily be performed in the 1-2ms window required for optical mapping, and thus the proposed method is completely feasible. Additionally, the topological specifications are quite robust; stimulation need only be applied in the general vicinity of the refractory boundaries. Even if these regions drift slightly during the computation time, the desired effect of the stimulus is still established.

The mechanism of defibrillation by teleportation was also used to explain the success

and failure of existing defibrillation methods. High-energy shocks automatically stimulate the necessary refractory contours of every spiral pair, while low-energy shocks do not and in general may generate additional spiral pairs. While we have only demonstrated this topological mechanism in 2D systems, generalization to 3D is trivial. Spiral waves generalize to scroll waves and rings with associated 1D singular filaments. These filaments are organized by refractory and excitable surfaces rather than contours. Just like in 2D, complete stimulation of the refractory surfaces joining filaments will eliminate the associated scroll waves, while partial stimulation results in the initiation of new waves. This generalization could be explored experimentally using the excitable Belousov-Zhabotinsky reaction [74]. With the necessary topological requirements for defibrillation elucidated, future low-energy defibrillation strategies may be developed that directly address the teleportation mechanism responsible.

# CHAPTER 4

# OPTIMIZING LOW-ENERGY ANTI-FIBRILLATION PACING: LESSONS FROM A CELLULAR AUTOMATON MODEL

## 4.1 Introduction

Cardiac fibrillation is often driven by reentrant spiral waves of electrical activity in the heart [38, 12, 13]. These patterns are defined by topological singularities near their center of rotation [11, 9, 52]. While traditional defibrillation applies a single strong shock to remove all singularities and reset the tissue [42], recent theory [75, 76] and experiment [77, 45, 78] has shown that the same result can be achieved with a series of weaker shocks. This therapy is known as low-energy anti-fibrillation pacing (LEAP). Extensive simulations have been performed analyzing LEAP using reaction-diffusion models in a heterogeneous domain [78, 76]. However, the complexity of such detailed models obscures the fundamental mechanisms responsible for successful defibrillation. In this Chapter, we show how significant insight can be gained from simulations in a very simple cellular automaton model. The model's minimal structure allows for easy tracking of individual spiral core singularities even in the presence of heterogeneous excitation. As a result, we are able to clearly demonstrate through simulation why certain pacing periods lead to more effective defibrillation. In spite of its simplicity, the model crucially retains the topological structure of more realistic models. By clarifying the role of topological constraints on the defibrillation process, we ultimately deduce a further optimized pacing strategy using a model-independent framework.

## 4.2 Cellular Automaton Model of LEAP

The simplest possible model of excitable media is the Greenberg-Hastings (GH) cellular automaton [79]. In this model, each lattice cell may occupy one of three states: resting, excited, or refractory. At each discrete time step, excited cells become refractory, refractory cells become resting, and resting cells become excited if a neighboring cell is excited. In two spatial dimensions, these rules are sufficient to support both unidirectional traveling waves and rotating spiral waves. In their original study, Greenberg and Hastings identified a conserved winding number that can be defined at each vertex on the lattice [80]. Spiral wave cores have a winding number of $\pm 1$ (with chirality given by the sign) and thus persist indefinitely, generating chaotic fibrillating states. An important consequence is that core singularities, and hence the spirals they belong to, must be eliminated for fibrillation to cease. This feature is analogous to the phase singularities of spiral waves in continuous systems [11, 9].

In order to gain insight into the defibrillation process, we study the GH model in the presence of stimulation (or shocking) which we implement by spontaneously making resting cells excited. Traditional defibrillation uses a single large shock to excite and reset all tissue in the heart simultaneously; while initially unexplained, it is now understood that this method succeeds by removing all reentrant spiral wave singularities [42]. This feature is retained in the modified GH model, as shown in Figure 4.1. In all figures, excited cells are red, refractory cells are yellow, and resting cells are turquoise. If every resting cell is excited, the winding number at every vertex must be zero, and no spirals can remain. This can be understood intuitively by considering the cores as phase singularities where all possible values of phase converge. By making all resting cells excited, the resting "phase" will necessarily be missing and singularities can no longer be present.

While theoretically a strong shock that excites the entire domain is always successful at removing spiral waves, clinical defibrillation is painful and can damage heart tissue in

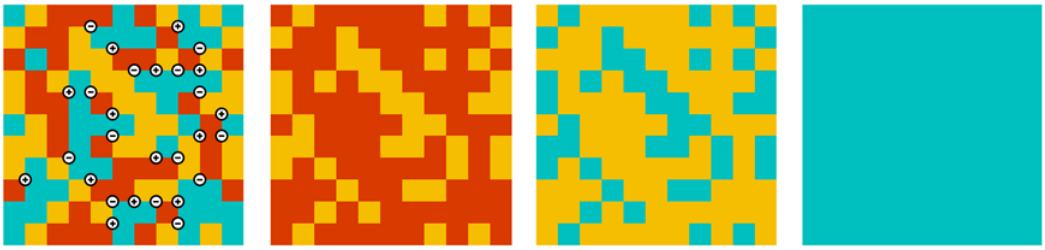

Figure 4.1: Complete defibrillation of a complex state containing many spiral singularities. Every resting cell is excited, resulting in immediate annihilation of every singularity. Singularities are identified by nonzero winding number and are marked with a $\pm$ corresponding to chirality. Excited cells are red, refractory cells are yellow, and resting cells are turquoise

the process [81]. There is therefore a strong clinical interest in developing effective low-energy defibrillation strategies. LEAP uses a series of multiple weak shocks to achieve the same results as traditional defibrillation [45, 78, 76]. Both methods exploit the virtual electrode phenomenon, in which far-field stimulation generates localized tissue activation around the heart's many natural heterogeneities [82, 83]. Stronger stimulation can recruit ever smaller heterogeneities, exciting a larger fraction of the total domain. Tissue response is therefore governed by size and density distributions of the heterogeneities as well as the stimulus strength. We characterize the tissue response for the cellular automaton model with a single parameter $p$—the probability for a resting cell to become excited during a shock. When $p = 1$, all resting cells are excited and complete defibrillation is recovered. For $p < 1$, a single shock, in general, will no longer completely defibrillate. We refer to $p$ as the shock strength, but it encapsulates both external stimulation strength and heterogeneity density in a simplified fashion.

For the original GH model, every $2\times2$ block of cell configurations can be categorized by the topological winding number at its vertex. This results in two distinct categories: spiral core patterns and non-core patterns. With the inclusion of the shocking procedure, non-core patterns can be further categorized as either vulnerable or invulnerable patterns. During a shock step, vulnerable patterns can be converted into core patterns, while invulnerable patterns cannot. Core patterns can also be converted to invulnerable patterns, in which

case the core's spiral is eliminated. Figure 4.2 shows this categorization for all unique $2 \times 2$ block patterns. Low-energy shocks can thus fail to defibrillate not only because they do not remove all existing spiral core singularities, but also because they may generate additional singularities. This effect has been documented in experiments on isolated rabbit and dog hearts [83, 84] and is closely connected to the S1-S2 initiation of spiral waves commonly demonstrated in computational models [62, 61]. Remarkably, members of the three categories share identical transition probabilities to the other categories given by the following transition matrix:

$$\begin{pmatrix} C_{t+1} \\ V_{t+1} \\ I_{t+1} \end{pmatrix} = \begin{pmatrix} 1-p & 2p(1-p) & 0 \\ 0 & (1-p)^2 & 0 \\ p & p^2 & 1 \end{pmatrix} \begin{pmatrix} C_t \\ V_t \\ I_t \end{pmatrix} \tag{4.1}$$

In section 4.5, we discuss how this structure is related to the underlying topology of singularities, and how it can be exploited to optimize low-energy pacing.

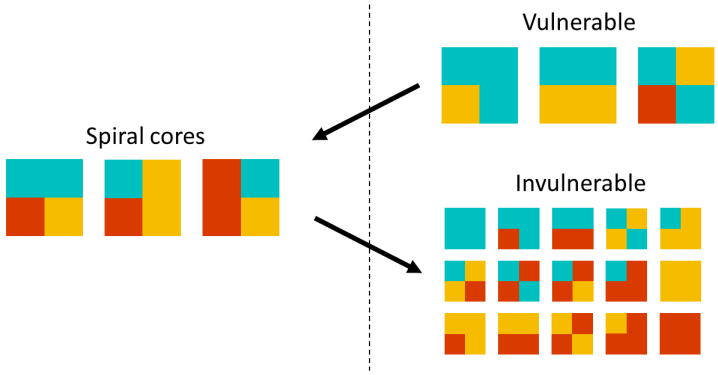


Figure 4.2: Categorization of all possible $2 \times 2$ block patterns up to reflections and rotations. Spiral cores (C) have nonzero winding number and generate persistent spiral waves. Vulnerable patterns (V) may be converted to cores by a shock of strength $p < 1$ while invulnerable patterns (I) are immune to such a conversion. Cores can be converted to invulnerable patterns yielding partial defibrillation.

LEAP is typically implemented by weak pacing at regularly timed intervals. We mimic this in our cellular automaton simulations as follows. First, we randomly initialize the cells

on a $N \times N$ domain, resulting in a complex state containing many spiral cores. We then apply a period $T$ of ordinary time-evolution steps followed by a single shock step with strength $p$. This sequence of $T + 1$ steps is then repeated until the total number of cores reaches a statistical steady state in which, on average, the number of cores generated by a shock balances the number of cores destroyed. To ensure that the total topological winding number is zero and cores exist in pairs of opposite chirality, we employ periodic boundary conditions. Figure 4.3 shows the beginning of a LEAP simulation with $N = 10$, $T = 4$, $p = 0.7$.

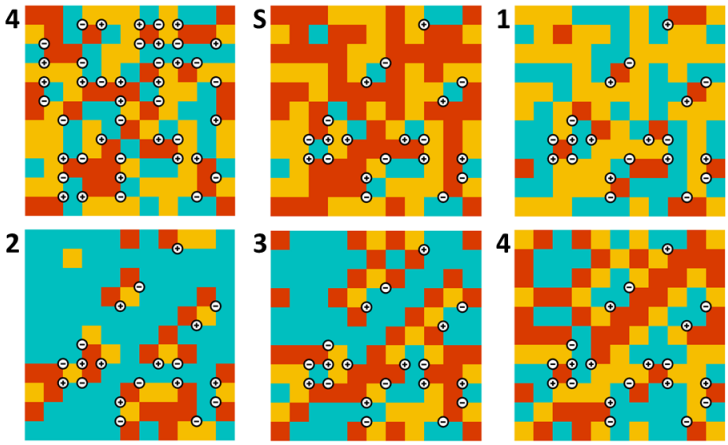


Figure 4.3: A full period of evolution for a LEAP simulation with $N = 10$, $T = 4$, $p = 0.7$. The shock step S reduces the total number of cores.

For a $2 \times 2$ domain, the average number of cores $\overline{W}$ generated from random initial conditions can be easily calculated by enumeration to be $\frac{32}{27}$. The statistical results from Figure 4.4 show that this result extrapolates to larger domains by scaling with the total area (or alternatively, number of vertices) such that the general result is

$$\overline{W}(N) = \frac{8}{27} N^2. \tag{4.2}$$

This provides a convenient extensive scaling for comparing results between domains of different sizes. In particular, we are interested in the statistical steady state as $N \to \infty$. Figure 4.5 shows the LEAP steady state number of cores scaled by Equation 4.2 for $T = 4$

as $p$ and $N$ are varied. By $N = 50$, steady state results already converge. For subsequent LEAP simulation statistics, we thus take $N = 50$ and normalize the number of cores by Equation 4.2 to obtain intensive results absent of finite-size effects.

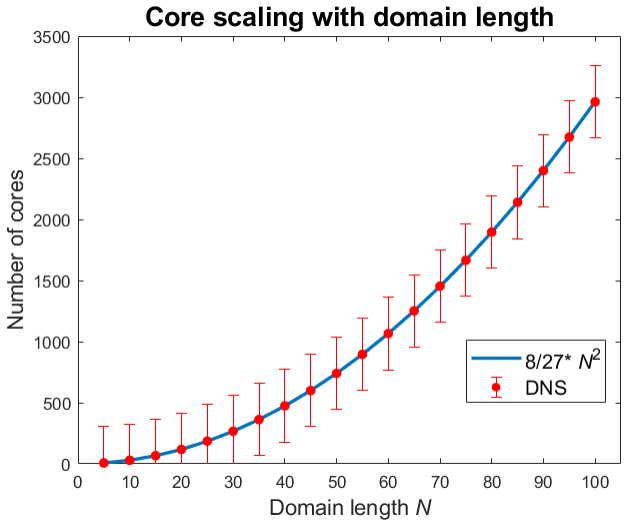


Figure 4.4: Number of cores from random initial conditions as domain size is varied. Statistical results show scaling proportional to the total domain area. Error bars are scaled by $1/N^2$ and also scale linearly with area.

Figure 4.6 shows the steady state results of LEAP simulations as period and shock strength are varied. While the average number of cores decreases with increased shock strength for all periods, certain periods perform particularly well. Period 4—the period of rotation for individual spirals—in particular is able to defibrillate in finite time when as little as 60% of tissue is excited per shock. Figure 4.7 shows the probability of successful defibrillation after 20 shocks and highlights the peak in efficiency near period 4.

### 4.3 Mean field theory predictions

With the addition of probabilistic LEAP shocking, the GH model may be formulated as a discrete-time Markov chain

$$\mathbf{s}_{t+T} = \mathbf{M}\mathbf{s}_t = \mathbf{P}(p)\mathbf{E}^T\mathbf{s}_t \tag{4.3}$$

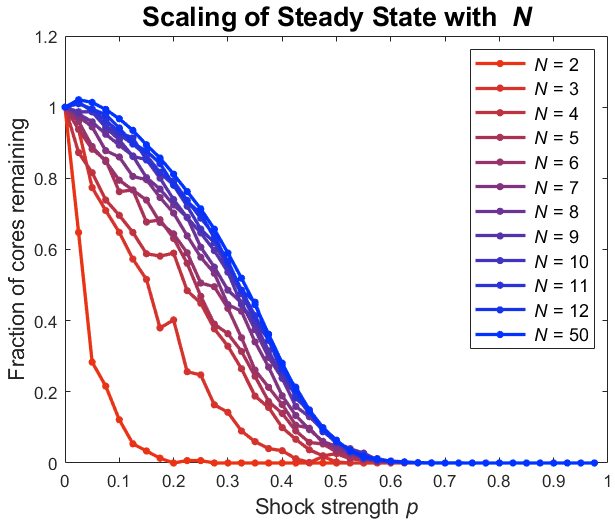


Figure 4.5: Steady state number of cores scaled by relation Equation 4.2 in LEAP simulation for $T = 4$. Results converge near $N \approx 50$.

where $\mathbf{s}_t$ is a vector containing the probability of each cell configuration at time $t$, $\mathbf{E}$ evolves the state by a single time step, and $\mathbf{P}$ applies the stochastic shock step. Because the system is ergodic, there exists a unique steady state probability distribution $\mathbf{s}_\infty = \mathbf{z}$ that the system tends to. While in principle $\mathbf{z}$ can be calculated directly from the Markov evolution matrix $\mathbf{M}$, the GH model has $3^{N^2}$ degrees of freedom, making the calculation extremely prohibitive for even small domain sizes. Additionally, we are interested in the statistics as $N \to \infty$, which can not be analyzed in this way. A computational technique commonly employed in such spatially extended statistical mechanics problems is self-consistent mean-field theory (MFT) [85].

By assuming the entire system is in the translationally invariant statistical steady state, MFT analyzes a small representative domain to find a self-consistent expression for this steady state. In the GH model, we take our representative domain to be either a $1 \times 1$ or $2 \times 2$ domain, with the latter giving a more accurate prediction [86, 85]. The self-consistency relation is then derived from Equation 4.3 as the following:

$$\mathbf{z} = \mathbf{P}(p)\mathbf{\Sigma}(\mathbf{z})\mathbf{z}. \tag{4.4}$$

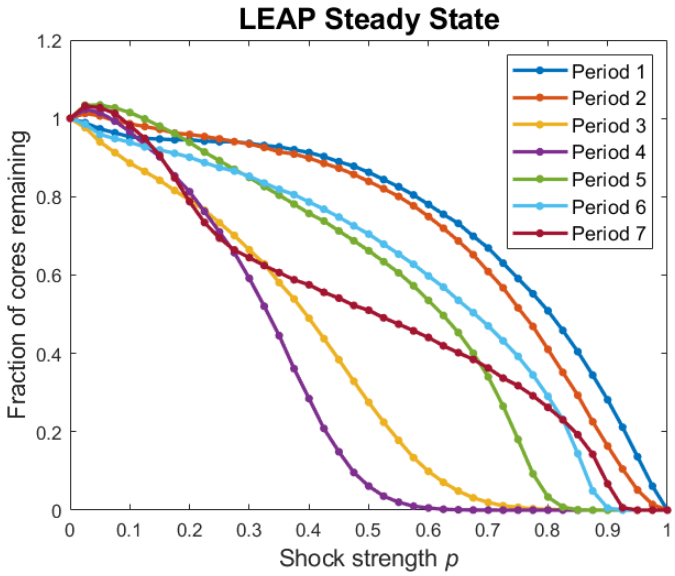


Figure 4.6: Steady state number of cores after many shocks in LEAP simulations as period and shock strength are varied.

For the $1 \times 1$ representative domain, the steady state $\mathbf{z}$ has only three components corresponding to the probability of an individual cell being at rest, excited, or refractory. The evolution matrix $\mathbf{\Sigma}$ evolves $\mathbf{z}$ according to the neighboring cells' states (see Figure 4.8). It therefore depends on $\mathbf{z}$ since the neighbors are also assumed to be in the steady state. The shock step has only a local effect, and is thus independent of $\mathbf{z}$. Equation 4.4 is solved numerically by iteration

$$\mathbf{z}_{n+1} = \mathbf{P}(p)\mathbf{\Sigma}(\mathbf{z}_n)\mathbf{z}_n. \tag{4.5}$$

with the initial guess $\mathbf{z}_0$ taken to be a uniform distribution. Once the converged steady state has been obtained for a given period $T$ and shock strength $p$, the average number of cores may be calculated by assuming every $2 \times 2$ domain is described by the steady state distribution and calculating the resulting average winding number.

Figure 4.9 and Figure 4.10 compare the steady state average number of cores $\overline{W}$ from the direct numerical simulations in Figure 4.6 to the MFT predictions for both $1 \times 1$ and $2 \times 2$ representative domains. As discussed previously, these results can be scaled to domains of any size using the relation in Equation 4.2. The larger representative domain is

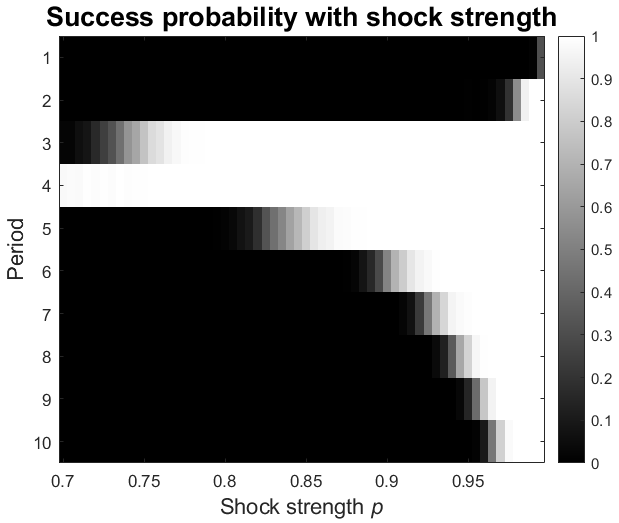


Figure 4.7: LEAP success probability after 20 shocks as period and shock strength are varied. A strong peak is localized near the $T = 4$ spiral rotation period.

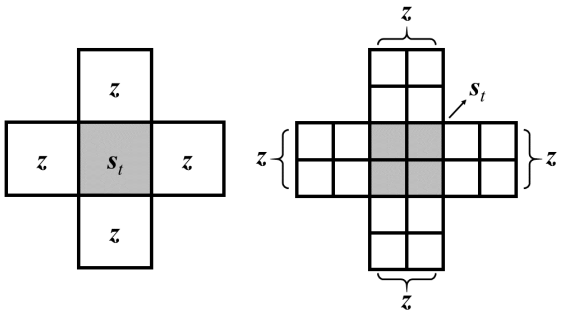


Figure 4.8: Representative domains for MFT calculations. States of shaded cells are calculated self-consistently through interactions with neighboring white cells in the steady state.

significantly more accurate for all periods, as expected. Predictions for period 4 and 7 are fairly inaccurate even for the $2 \times 2$ MFT. One possible explanation is that a phase transition occurs as $\overline{W}$ tends to zero at finite $p$; MFT is notoriously inaccurate near critical points due to the neglect of fluctuations [87]. Alternatively, better agreement may simply be achieved with larger representative domains. Longer pacing periods in principle allow for excitation waves to propagate larger distances—an effect which cannot be captured on small domains.

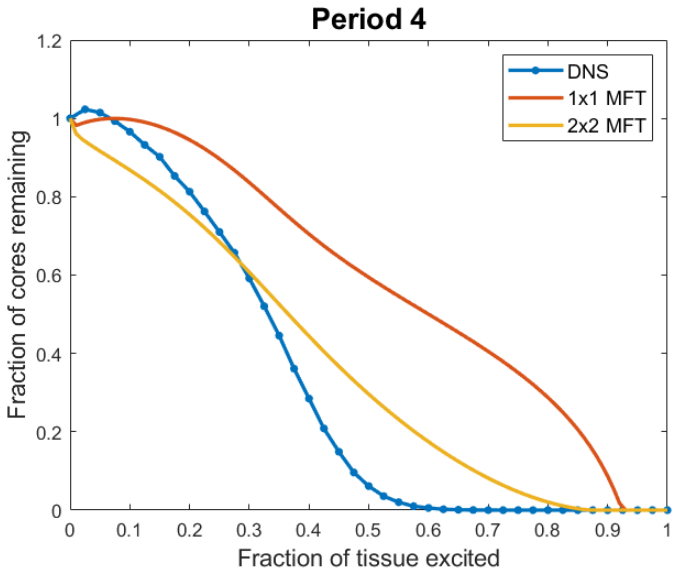


Figure 4.9: MFT steady state predictions compared to direct numerical simulation for period 4 pacing.

### 4.4 Origin of an optimal pacing period

A commonly reported feature of LEAP in both simulation [78, 76] and experiment [45, 78, 42] is the presence of an optimal pacing period close to either the dominant period of fibrillation or, equivalently, the period of spiral rotation. As was demonstrated in section 4.2, this feature is reproduced even in the highly simplified GH model which suggests that the mechanism responsible is a generic feature of all excitable systems. Previously no explanation for this apparent resonance has been provided. Using the GH model, we now show through simple examples how it arises as a competition between two mechanisms intrinsic to generic excitable media.

From Figure 4.6, we see that pacing with $T = 7$, $p = .3$ is highly ineffective, reducing the number of cores to only 60% of the starting number. An entirely different result is achieved when the system is initialized in the the uniform rest state, however. Figure 4.11 shows how the shock is unable to generate any new cores due to a lack of refractory cells. By $t = 6$, the system has returned to the uniform rest state a full time step before the next shock is applied. As a result, the process repeats and no new cores are created.

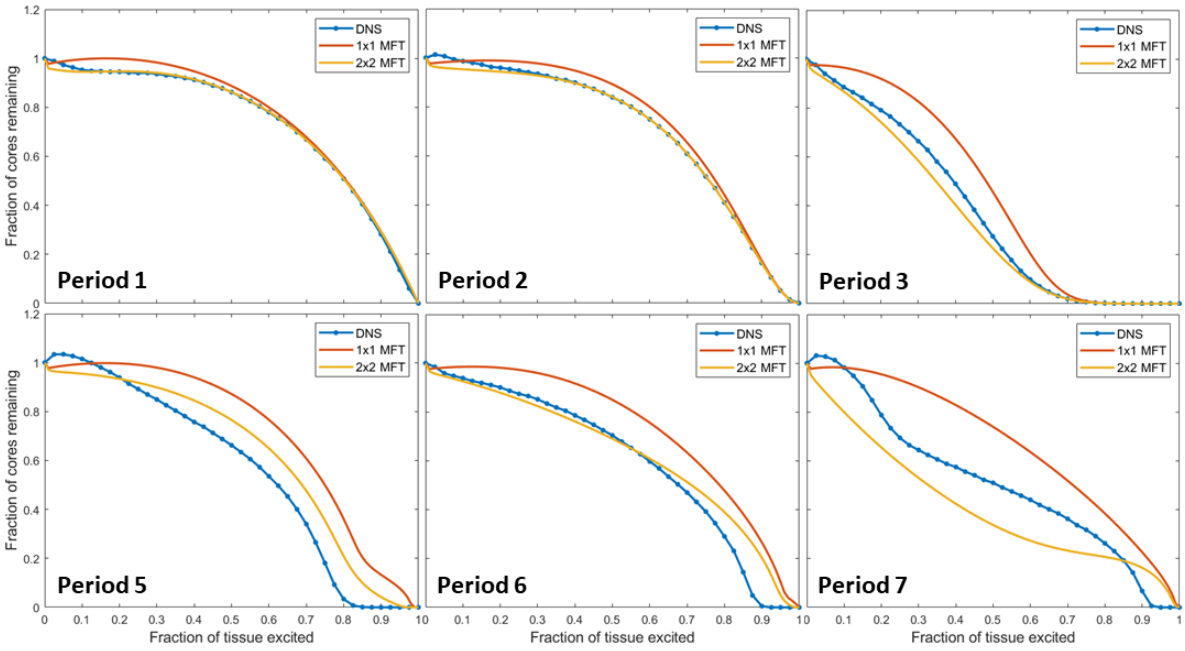


Figure 4.10: MFT steady state predictions compared to direct numerical simulation for additional pacing periods.

Because the system is ergodic, it will eventually converge to the steady state reported in Figure 4.6, although this metastable sequence is extremely long-lived. Figure 4.12 shows how the presence of even a single refractory cell can rapidly trigger a transition to the steady state. The first shock initiates a small number of cores localized to the perturbation. During the time preceding the next shock, the cores generate expanding target waves which contain many additional vulnerable patterns. The next shock thus creates even more cores along the back of this expanding wave. This process repeats, resulting in a nucleation of new cores surrounding the initial perturbation.

By allowing the excitation of the previous shock to fully dissipate before the next shock is applied, longer-period pacing prevents the creation of new cores associated with transient refractory regions. When cores are present, however, the associated vulnerable regions persist and grow as subsequent shocks generate new cores.

Figure 4.13 shows the results of pacing the perturbed state with a shorter period of $T = 4$. The first shock once again initiates new cores near the perturbing refractory cell. By the time the next shock is applied, the original cores have barely begun to form target

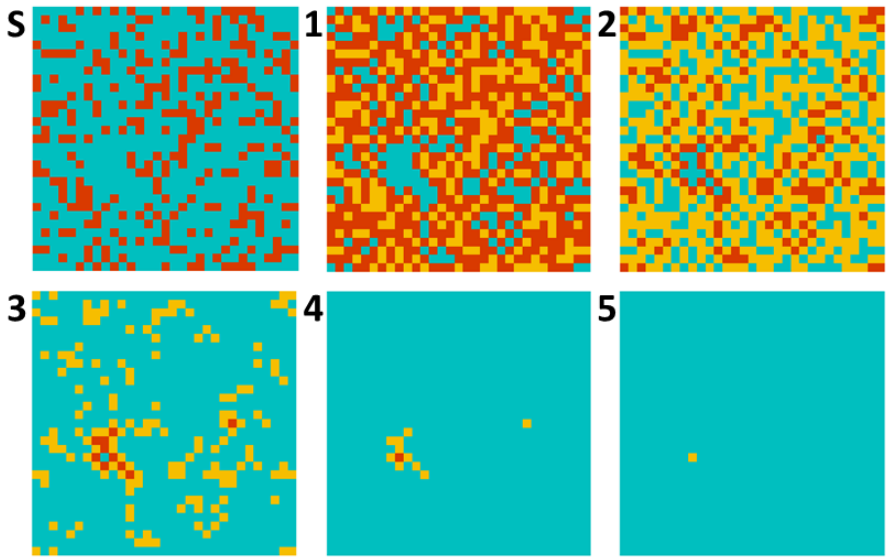


Figure 4.11: LEAP pacing with $T = 7$, $p = .3$ starting from the uniform rest state. The entire domain returns to rest before the next shock is applied and no new cores can be created.

patterns and do not produce extra vulnerable regions. However, a number of transient refractory cells still remain from the previous shock. The associated vulnerable patterns of these transients trigger the generation of many new cores uniformly throughout the domain.

These two examples demonstrate how pacing periods that are either too long or too short are both susceptible to generating new spiral cores and thus ineffective at defibrillating. The optimal period must be short enough to suppress localized nucleation around existing cores but long enough to allow transient refractory cells to recover. A useful quantity to consider in light of these mechanisms is the mean dissipation time. This is the average amount of time for cells to return to rest after a shock is applied. For shocks of moderate strength, rest cells are either shocked with probability $p$ and take two time steps to recover, or else are not shocked but are immediately excited by a neighbor at the next time step and thus require three time steps to recover. The resulting mean dissipation time is given by

$$\tau \approx 2p + 3(1-p) = 3 - p. \tag{4.6}$$

Figure 4.14 shows that this rough estimate is in excellent agreement with direct numerical

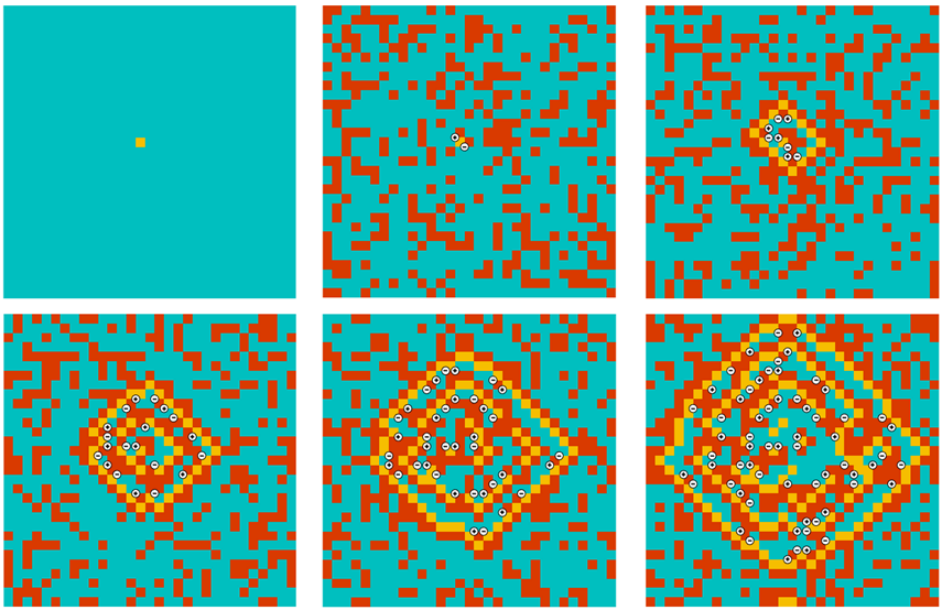

Figure 4.12: LEAP pacing with $T = 7$, $p = .3$ starting from the uniform rest state with a single perturbing refractory cell. Each shock generates new cores nucleating from the initial perturbation. Seven time steps and a single shock step elapse between each plotted frame after the first.

simulation by $p \approx .5$. As shock strength approaches 1, the mean dissipation time is limited by the two steps a single cell takes to recover. Thus, for moderate shock strength, $T = 3$ is the fastest pacing period which avoids core creations due to the transients of previous shocks. Figure 4.15 shows the extremely efficient progression of $T = 3$ pacing for $p = .8$. After only a few shocks, all cores are removed.

Rather than a resonance phenomenon, we see that the optimal pacing period emerges from a competition between spiral creation mechanisms occurring at short and long periods. Nevertheless, the optimal period and the spiral period do appear correlated. One possible explanation is that the optimal period and spiral period are both roughly set by the mean dissipation time; in order for a spiral wave to undergo a full rotation, the surrounding tissue must complete a full cycle of recovery. A similar condition is required for efficient pacing.

If there is no true resonant response at the spiral period, as our analysis suggests, non-periodic pacing has the prospect of providing more efficient defibrillation by allowing for more sophisticated shocking protocols. In the following section we explore this possibility

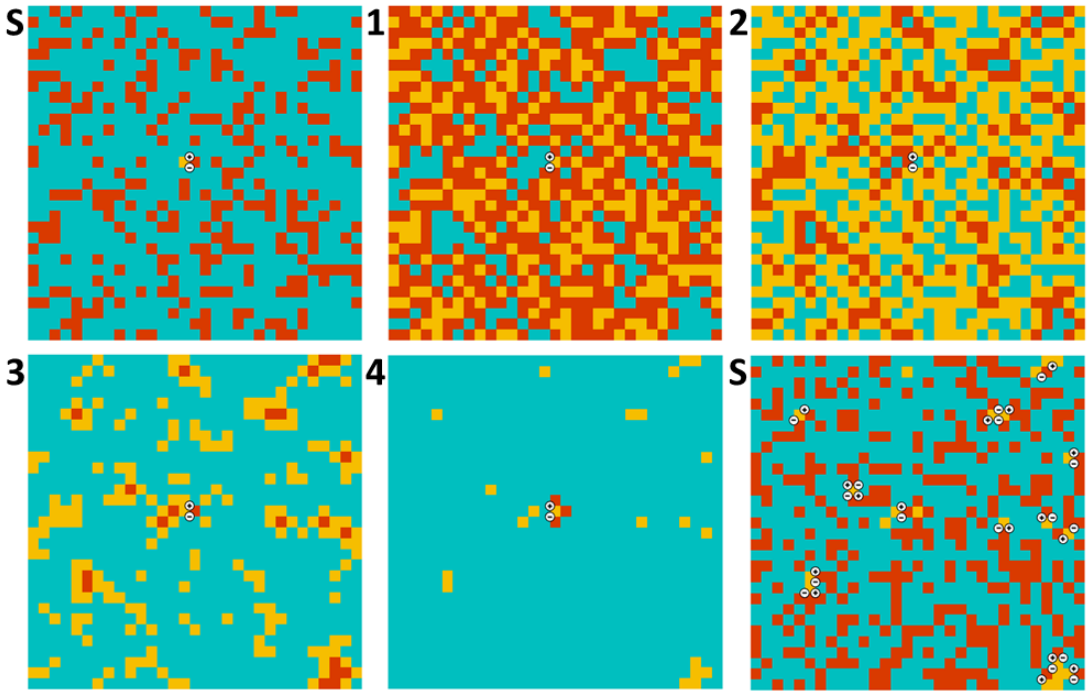


Figure 4.13: LEAP pacing with $T = 4$, $p = .3$ starting from the uniform rest state with a single perturbing refractory cell. No nucleation is observed but many new cores are generated near unrecovered tissue.

and indeed find that allowing the period between shocks to vary leads to improved efficiency.

### 4.5 Topologically optimized pacing

Our analysis thus far suggests that optimal low-energy pacing is achieved not by matching the spiral period, but by pacing at times which minimize the probability of creating new spiral wave singularities. Although fixed-timing pacing is optimized when the period approximately equals the mean dissipation time, in general the time for tissue to relax after a shock varies. Moreover, the probability of creating new singularities at a given time depends on the detailed spatial configuration and evolves irregularly due to the chaotic nature of fibrillation. A truly optimal pacing strategy must constantly adapt its timing accordingly. In this section, we will show how topological analysis can be used to determine when an applied shock will be most effective. To this end we first describe the general features

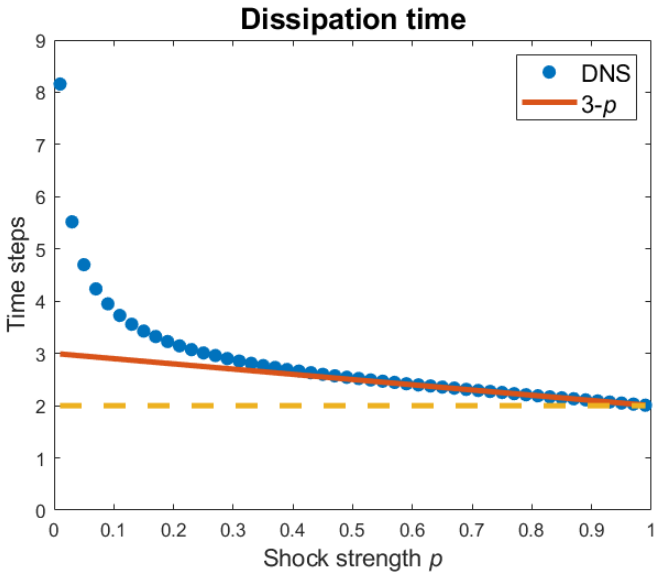


Figure 4.14: Average amount of time for cells to return to rest after a shock is applied.

of topological analysis in continuous excitable media and how it may be extended to the discrete cellular automaton model.

The topology of spiral wave dynamics has often been characterized by a local phase variable, hence the terminology of "phase singularity" [11, 12]. However, modern work on excitable systems has shown that a more natural topological description is obtained by tracking the regions of tissue that are excited or refractory, respectively [49, 48, 55, 56, 88]. In two-dimensional systems, these regions are bounded by one-dimensional contours that are the primary objects of interest. As a result of continuity, each contour either forms a closed loop or terminates at a boundary [9]. Singularities are located at the isolated points where the excited and refractory contours intersect.

The excited and refractory contours can be further subdivided into back and front segments to capture the propagating nature of the system dynamics. Excited fronts and refractory backs are formed where the respective contours enter regions in the rest state. Excited backs and refractory fronts are formed in the opposite cases, leading to a total of four segments types [48]. Propagating waves lead with an excited front that spreads into resting tissue, and is followed (in order) by a refractory front, an excited back, and finally a refrac-

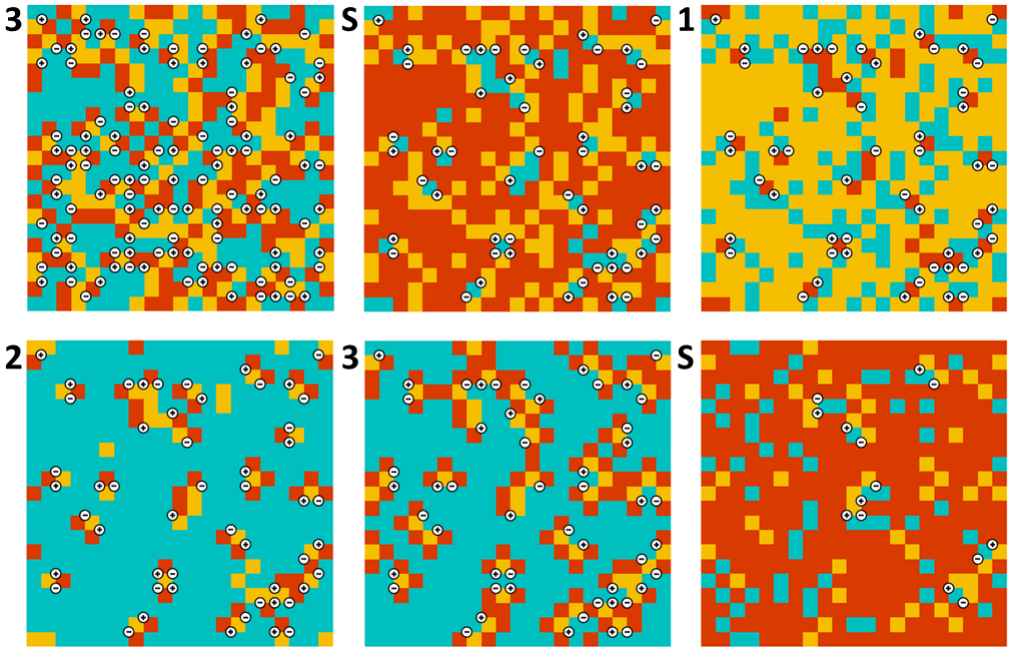


Figure 4.15: LEAP pacing with $T = 3$, $p = .8$. Cores are efficiently eliminated with minimal reinitiation.

tory back that connects back to the rest state. Figure 4.16 shows how the contour segments can be defined in the GH model along cell edges. Since excited and refractory regions cannot overlap in this discrete model, the excited back and refractory front lie along the same edge.

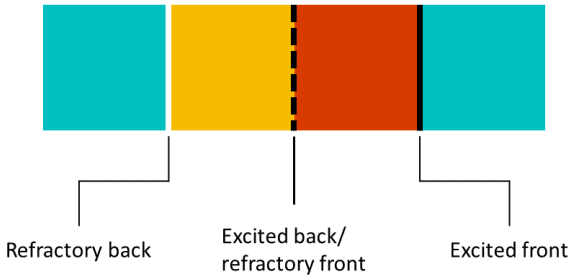


Figure 4.16: Organizing topological contours (white, dashed black, and black) defined along edges between neighboring cells.

Figure 4.17 shows the contours and singularities for an arbitrary fibrillating state and demonstrates a significant topological feature: each singularity is connected by contour segment to a singularity of opposite chirality. This is actually a manifestation of conservation of topological charge [9, 48, 49], which states that spiral core singularities can only be

created or destroyed in oppositely rotating pairs.

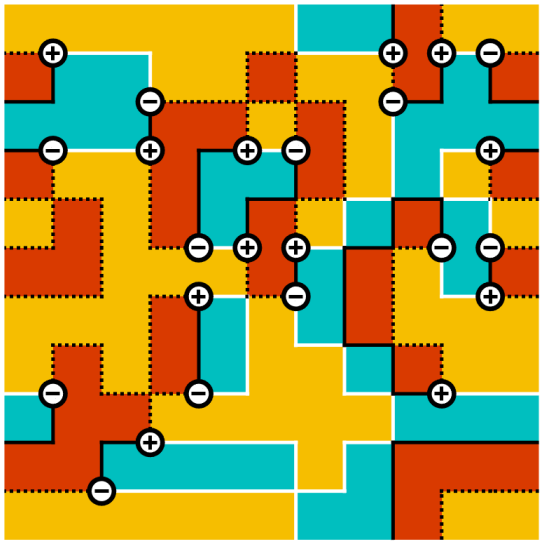

Figure 4.17: Topological contours and singularities plotted for an arbitrary fibrillating state. White lines are refractory backs, black lines are excited fronts, and dashed black lines are excited backs/refractory fronts.

In particular, it was recently shown [88] that the necessary condition for eliminating a pair of singularities is to excite along the refractory back contour joining them. This instantaneously removes the two singularities and converts the reentrant spiral waves into a transient radially propagating wave. If only part of the joining refractory back contour is excited, the singularities will in general be transported along it but will not be eliminated. Sufficiently irregular excitation leads to the creation of entirely new pairs of singularities via the S1-S2 creation mechanism [61]. Each of these cases is demonstrated in Figure 4.18 for a single pair of connected singularities in the GH model. Successful single-shock defibrillation thus requires the excitation of every rest cell adjacent to a refractory back contour in order to annihilate every pair of singularities. When all rest cells are excited, as in Figure 4.1, this condition is automatically met without a detailed understanding of the underlying topology. However, the same result can clearly be achieved by shocking a smaller number of cells.

Excitation of the refractory back contours is also the necessary condition for defibrillation in one-dimensional cables. In this geometry, fibrillation is represented by reentrant

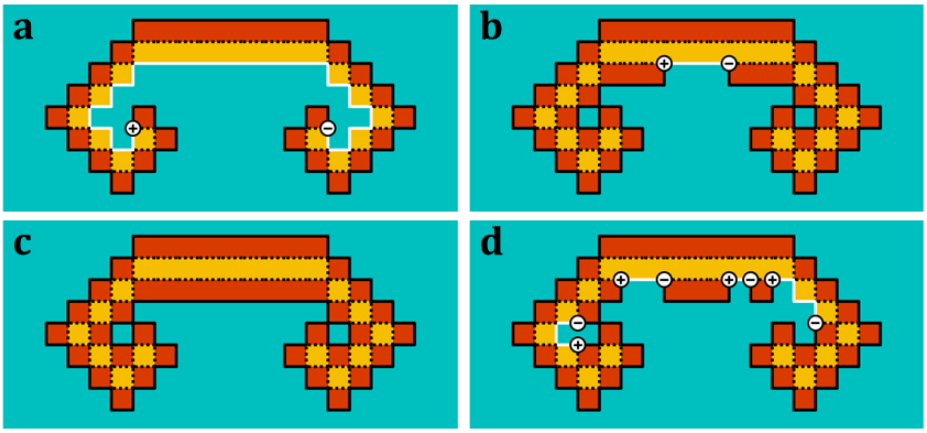


Figure 4.18: Elimination of singularities via contour stimulation. (a) Initial pair of oppositely rotating singularities joined by all three topological contours. (b) Both singularities are transported closer together by stimulating continuously along the white refractory back contour. (c) Stimulating the entire refractory back contour causes the two singularities to mutually annihilate. (d) Discontinuous stimulus of the refractory back contour from a shock with $p < 1$ leads to the creation of several new pairs of singularities.

traveling waves and can be topologically characterized with a global winding number [89, 49]. Figure 4.19 shows the evolution and subsequent defibrillation of a configuration with initial winding number $-2$ corresponding to two leftward-traveling waves and a bidirectional wave with zero net winding number. At the fifth time step, the refractory back contours are stimulated and generate two rightward-traveling waves which then collide and annihilate with the original waves.

While the topological contour framework clearly dictates the necessary conditions for defibrillation and explains the success of domain-wide stimulation, it also explains why low-energy multi-shock defibrillation can fail. If stimulus along the refractory back contour is not uniform, new pairs of singularities are created as demonstrated in Figure 4.18(d). In this example, the low-energy shock generated new singularities without removing any of the originals, leading to a worse state of fibrillation. The vulnerable patterns described in section 4.2 are a manifestation of this property; each contains refractory back contours that allow for the stimulated creation of new singularities.

Although defibrillation is traditionally implemented by excitation of tissue (primarily

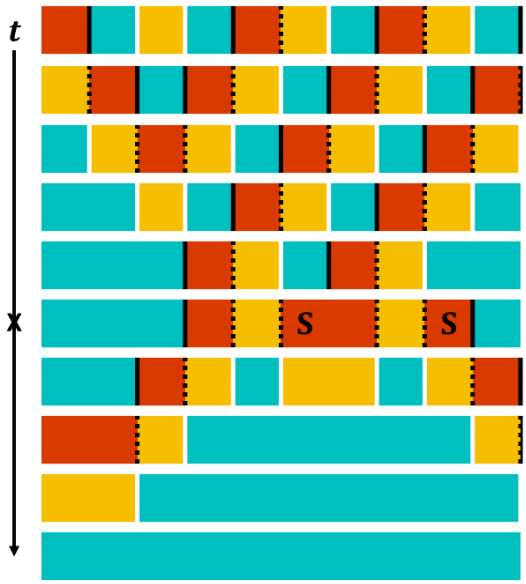


Figure 4.19: Defibrillation in a one-dimensional periodic cable. The initial configuration contains two leftward-traveling waves and a bidirectional wave representing reentrant fibrillation. At the marked time step (cross), refractory back contours are stimulated leading to defibrillation.

due to the asymmetric response of virtual electrodes) rearrangement and annihilation of singularities has also been shown to be possible by deexciting cells [49, 88]. In fact, because external stimulus of the GH model is independent of the rules of regular time evolution, manipulation of singularities is possible by converting any cell state to any other. The result of each conversion is displayed in Figure 4.20. For example, converting a singularity-adjacent rest cell to a refractory cell will transport the singularity along the nearby excited front contour. For a given fibrillating configuration such as that of Figure 4.17, a truly optimal defibrillating stimulus could be designed by finding the smallest number of cells necessary to convert in order to annihilate every singularity. This essentially amounts to finding the shortest contour between each pair of singularities and applying the proper conversion from Figure 4.20 in order to mutually annihilate them. Because singularities are almost never paired exclusively to one other singularity, this problem becomes quite complex as the number of singularities increases.

Having described how an exciting stimulus interacts with the topological refractory

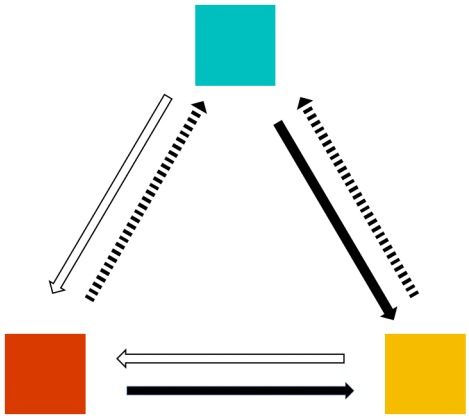

Figure 4.20: Diagram of different state conversions leading to transportation of singularities along a given contour. Arrows directed between two states represent conversion while arrow color represents contour the singularity will move along.

back contours to either increase or decrease the number of spiral core singularities, we now show how these properties can be used to design an optimized pacing scheme. The goal of a low-energy defibrillating shock is to minimize the number of new singularities created while maximizing the number that are eliminated. By monitoring the refractory back contours, shocks can be applied at specific times to achieve this goal.

Our proposed pacing strategy is motivated by the singularity creation mechanism present in e.g. Figure 4.18(d). In order to completely defibrillate, the refractory back contours joining singularities must be stimulated continuously. Any discontinuities due to the random profile of LEAP shocking will typically generate new pairs of singularities. In fact, the probability of successfully annihilating two singularities joined by a contour of length $L$ is $p^L = e^{\ln(p)L}$ which decreases exponentially with increasing $L$. In light of this fact, a topologically motivated strategy is to shock whenever the total length of the refractory back contours reaches a local minimum. This condition ensures that pairs of singularities are close together and can be annihilated by exciting only a few consecutive cells. Additionally, transient refractory cells from previous shocks contribute significantly to the total contour length. A local minimum in the total length thus indicates that the transients have fully dissipated, and so a new shock will not create new singularities. Since the tracking of contours has been successfully demonstrated in both detailed simulation [55] and ex-

periment [56] using only noisy voltage data, this defibrillation method is also universally applicable; this reflects the extremely general nature of the topological analysis.

For comparison, we also demonstrate a second pacing strategy that exploits the Markov formulation of the shock step in terms of the core, vulnerable, and invulnerable patterns. If $C$, $V$, $I$ are the numbers of each type of pattern in a configuration, then the average change in cores after a shock is given from Equation 4.1 by

$$\Delta C = -pC + 2p(1-p)V. \tag{4.7}$$

A simple greedy defibrillation algorithm then consists of computing $\Delta C$ and shocking when it is negative, i.e. when the shock will, on average, decrease the total number of cores. While effective, this method is limited to the GH model for which an explicit Markov representation exists. However, it conveniently constitutes another topologically informed pacing method that can be compared to fixed-period pacing.

Figure 4.21 shows the steady state fraction of cores for both the Markov and contour methods compared to the original constant period LEAP. Both methods outperform spiral period pacing and successfully defibrillate at a lower shock strength.

Figure 4.22 and Figure 4.23 show the average number of shocks and amount of time, respectively, for the four most effective methods to completely defibrillate. The Markov method typically requires more shocks but consistently defibrillates in the shortest time. The contour method is as effective as period pacing 3 for stronger shock strengths but significantly outperforms it at lower strengths.

This latter relationship can be understood from Figure 4.24 which shows the relative frequency of time steps between shocks in the contour tracking method. Initially, shocks occur every three or four steps with similar frequency. By mixing the two timings, the method outperforms constant period pacing at either individual period. As shock strength grows and the mean dissipation time decreases, shocking every three steps becomes more favor-

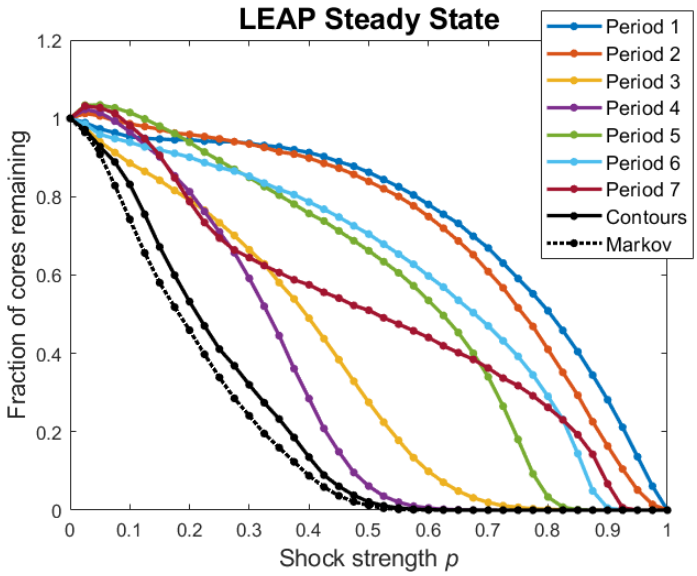


Figure 4.21: Steady state number of cores in LEAP simulations including Markov and contour pacing strategies.

able. As shock strength increases further still and the mean dissipation time approaches the minimum of two steps, three-step shocks begin to be replaced by two-step shocks. This progression also demonstrates the contour tracking method's greatest strength: the ability to adapt to different system parameters automatically. Unlike traditional LEAP, which needs to be manually optimized to a particular and non-obvious pacing period which varies with field strength [76], contour tracking is system-independent and can pick out optimal shock timing on the fly from topological information.

## 4.6 Conclusions and Open Questions

In this Chapter, we have explored the generic phenomenology of far-field low-energy defibrillation using a cellular automaton model of excitable media. Despite its extreme simplicity, this model obeys the same crucial topological rules as more sophisticated continuum models; fibrillation is produced by the persistence of phase singularities at the cores of spiral waves and ceases only when every pair of singularities is mutually annihilated. From simulations of periodic low-energy pacing, the origin of an optimal pacing period was

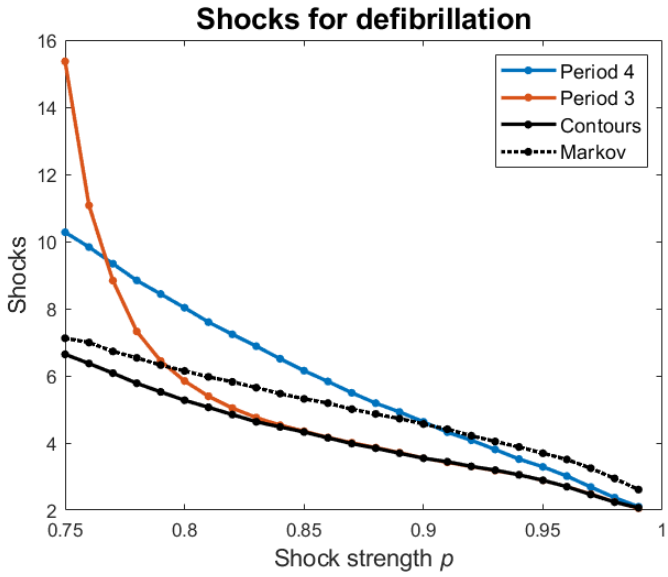


Figure 4.22: Average number of shocks to reach defibrillation for the four most effective pacing protocols.

identified as arising from the competition between two spiral creation mechanisms—one occurring at short period pacing, and one for long. Pacing slowly allows existing spirals to propagate and produce large vulnerable regions where new singularities may be created. Pacing faster than the tissue can return to rest from the previous shock results in many new singularities created along the transient refractory regions. Optimal pacing is achieved by pacing as soon as the refractory transients have dissipated. While the GH model lacks many realistic features such as curvature and spiral drift, it reproduces the same exponential scaling of defibrillation success with refractory boundary length found in continuous reaction-diffusion models $P(\text{success}) = e^{-k\,L}$, where the scaling factor $k$ depends on applied field strength [90]. As such, it captures the fundamental phenomenology of defibrillation in a course-grained fashion by embedding details in the shock-strength parameter $p$ while maintaining the system's intrinsic topology.

We also demonstrated a novel pacing scheme based on established topological analysis of spiral wave turbulence. By tracking the topological contours linking singularities and shocking when their length is short, spiral creation is minimized directly and the resulting shock timing is consistently optimized. Our simulations suggest that this method outper-

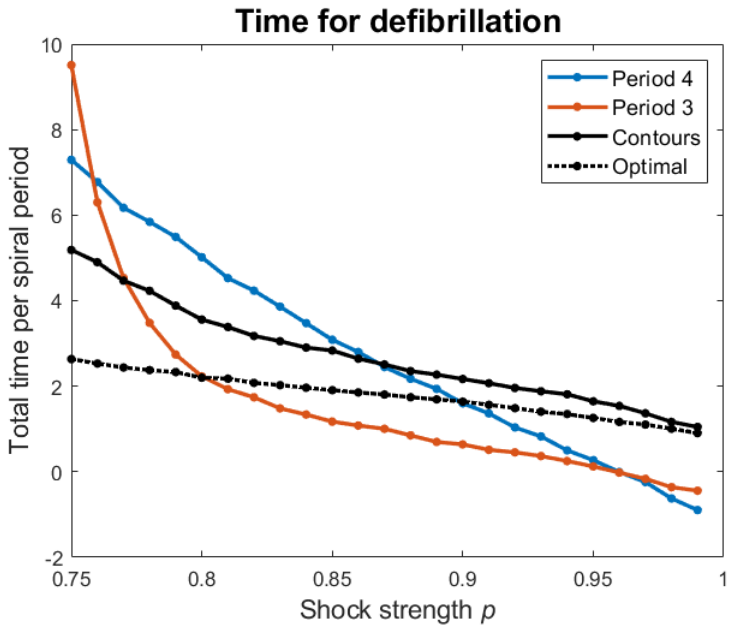


Figure 4.23: Average time in units of spiral period (four time steps) to reach defibrillation for the four most effective pacing protocols.

forms traditional fixed-period pacing and defibrillates at a lower shock strength. Most significantly, the topological nature of this strategy makes implementation in clinical experiment feasible; successful tracking of contours from experimental voltage data has been demonstrated in previous studies. While it is not possible to image the full 3D electrical activity of a real heart, the optimized procedure may still be implemented by considering only 2D surface recordings. Excitation in the bulk of the heart ultimately generates refractory contours on the outer boundary. Gradual elimination of 3D scroll waves by LEAP is thus still optimized by considering the length of these boundary contours. One relevant 3D phenomenon not captured by the GH model is filament tension of the reentrant scroll waves [91]. While positive tension would cause filaments to shrink and increase the probability of low-energy defibrillation, negative tension may cause filaments to expand and break, hindering the process [92]. Additionally, moderate resolution surface recordings would be required to sufficiently capture the activation topology. If localized refractory regions cannot be properly imaged, timing optimization may become unreliable compared to traditional fixed-period LEAP pacing.

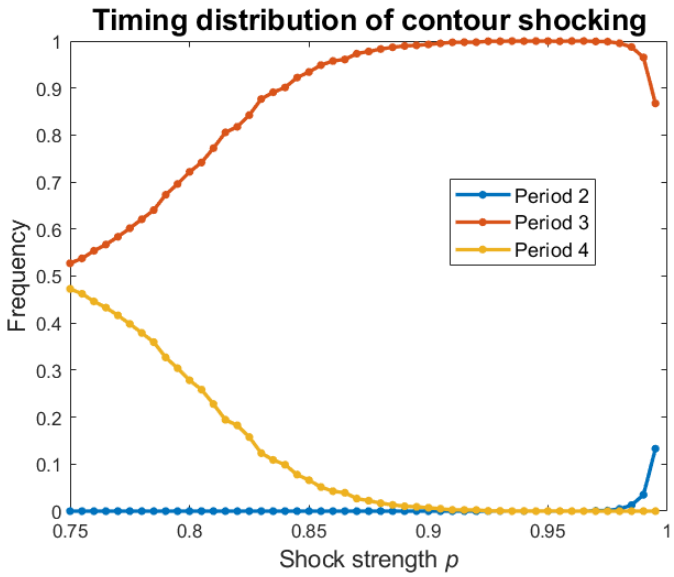


Figure 4.24: Relative frequency of number of time steps between shocks during the contour tracking protocol.

# CHAPTER 5
# CONCLUSION AND FUTURE PERSPECTIVES

In Chapters 3 and 4 of this thesis, strategies for eliminating persistent cardiac fibrillation were demonstrated in models of excitable cardiac tissue. Behavior in these models was characterized topologically, allowing for the location of spiral wave singularities that maintain fibrillation. Additionally, it was shown how spiral waves could be eliminated by stimulating along the organizing topological contours. Specifically, excitation of the refractory back joining two spirals was argued to be the minimal perturbation required to induce mutual annihilation of the corresponding topological singularities. In both single-shock and multi-shock strategies, these refractory back regions must be targeted (directly or indirectly) in order to achieve successful defibrillation.

In the discrete cellular automaton model of Chapter 4, it is possible to specify exactly the regions comprising the refractory back. If and only if that unique set of cells are excited will the reentrant singularities be instantaneously annihilated. The continuum models, on the other hand, are quite flexible in their topological specification. A variety of different indicator functions can be used to define the refractory back region, and it is straightforward to find through trial and error a stimulus strength and thickness that result in consistent defibrillation. This lack of uniqueness ultimately originates from the ambiguity in assigning an emergent property (namely refractoriness) to a local system state. The same issue does not arise when assigning a local phase to an extended oscillatory medium. While the topological indicator function framework is extremely robust in practice, it is still worth exploring alternative frameworks which could specify exact conditions for defibrillation. This amounts to shifting from a topological approach to a dynamical systems approach.

Rigorous conditions for defibrillation can be defined by considering the basins of attraction of the multispiral fibrillating state and the uniform rest state. In order to defibril-

late, a perturbation must force the system away from the first stable state and toward the other. This caricature of excitable media as a bistable system is of course complicated by the infinite dimensionality of the PDE system; determining the basin of attraction of an infinite dimensional solution even numerically is an exceedingly difficult task. However, instructive progress in this direction has been made for some simple examples in excitable systems. The best studied example is the so-called ignition problem for propagating waves in one spatial dimension.

In the ignition problem, one attempts to determine the set of initial conditions which lead to the stable propagating wave solution [93, 94]. Initial conditions that are "too small" will decay to the uniform rest state. Above a certain threshold, the stable propagating pulse will form and persist. A key element in the structure of this problem is the so-called slow wave solution. This additional solution is an unstable traveling wave with a velocity that is characteristically slower than that of the stable traveling wave [95]. The slow wave acts as a high-dimensional separatrix dividing the basins of the stable fast wave and uniform rest states; such a saddle solution must exist for any multistable system. Remarkably, the slow wave has only a single unstable mode. As a result, the associated one-dimensional unstable manifold must be traversed in order to cross over from one basin to the other. By parameterizing this manifold [96, 97], a single coordinate can be introduced which maps any configuration to a signed "distance" from the slow wave. The sign of this coordinate then dictates which basin of attraction the configuration lies in. A local approximation of this calculation was undertaken in [94].

Inversion of the ignition problem (referred to as the quenching problem) can be treated as a very elementary model of defibrillation. The question of what perturbations to the stable fast wave cause a transition to the uniform rest state may again be answered rigorously using the parameterization of the slow wave's unstable manifold. It is also worth noting that the fast wave can be considered to have a nonzero topological winding number differentiating it from the uniform rest state [98] and so the similarity of the quenching problem to

defibrillation is more than superficial. Finally, the parameterization method is well-suited for optimized control schemes [4] and could in principle be used to determine the minimal spatiotemporal perturbation required to transition from the reentrant fast wave to the "healthy" rest state. It remains to be seen if such an optimization scheme will reproduce the topologically motivated strategy of perturbing near the refractory back demonstrated in Figure 4.19.

The same type of dynamical analysis used in the ignition problem can be applied in two spatial dimensions to isolated stable spiral wave solutions; as before, a separatrix must exist to divide the stable spiral from the uniform rest state. While such a saddle solution has yet to be obtained explicitly, its existence is implicitly identified by the following observations. When a stable spiral wave is sufficiently close to a no-flux boundary, the interaction induces a drift in the spiral rotation [99]. At moderate distances, the spiral is repelled from the boundary. Below a critical distance, however, the spiral becomes attracted to the boundary until it collides with it and extinguishes [100]. If the spiral was located exactly at the critical distance separating attraction and repulsion, it would stay perfectly fixed; this configuration, made periodic by the spiral's rotation, forms the saddle state. Mirroring this solution about the boundary produces an equivalent saddle state separating a stable pair of spirals and their mutual annihilation leading to the uniform rest state. Parameterization of this saddle state's unstable manifold could be performed to once again determine the exact conditions for perturbing the stable spiral state into the stable rest state. Such an analysis may be more difficult if the saddle state has multiple unstable modes, however.

Although analyzing the organizing saddle states is a promising strategy for simple examples like individual traveling or spiral waves, it quickly becomes infeasible for complex states. Complications can arise even in the one-dimensional ignition problem. For example, in certain parameter regimes additional saddle states may appear [95]. In both one- and two-dimensional systems, stable states containing multiple waves exist; how might saddle solutions be identified for these configurations, and how are they connected to the single-

wave saddle? Finally, in realistic cardiac models, spirals spontaneously undergo breakup and annihilation with sufficient irregularity that the fibrillating state eventually extinguishes on its own [101]. These systems lack saddle solutions entirely, as every configuration lies in the basin of attraction of the rest state. Perturbing these transiently chaotic states can still lead to more rapid defibrillation than naturally occurs [102], but how exactly configurations are organized in terms of their lifetimes is not obvious. Evidently, many open questions remain in the dynamical theory of excitable media. Perhaps the most challenging question, however, is to what extent dynamical organization is governed by topological structure. The topological arguments used in Chapter 3 of this thesis clearly and unambiguously, if not quantitatively, explain how dynamical transitions between states may be induced. How exactly such topological rules may be derived from a dynamical theory remains a considerable outstanding challenge.

# Appendices

# APPENDIX A

# CALCULATION OF THE ORDER PARAMETER FOR CHAPTER 2

Two key observations from the discrete formulation allow us to proceed in calculating the thermodynamic limit of the order parameter for a given disorder distribution. First, the steady-state phase of the order parameter is linear in space, i.e. $\arg(Z_j) = \alpha j$. Since $\alpha$ is an arbitrary constant, it can be set to zero. Second, $|Z_j|$ is observed to be independent of $j$ in steady state. We can therefore choose to evaluate $Z(x)$ arbitrarily at $x = 0$ and set its phase to zero. Equation 2.15 then simplifies to

$$\begin{aligned} \dot{\Delta} &= \omega - M(x)\sin\Delta, \\ M(x) &= (1 - x/2)KR \end{aligned} \tag{A.1}$$

where $R = |Z(0)|$.

In the spirit of Kuramoto's solution to the Kuramoto model [103, 1], we seek stationary solutions of Equation 2.22 assuming a constant value of $R$. Oscillators with small disorder will have their phase entrained to the equilibria of Equation A.1 such that

$$\begin{aligned} \rho(\Delta, \omega, x) &= \delta\left(\Delta - \arcsin\frac{\omega}{M(x)}\right) g(\omega), \\ |\omega| &\leq M(x). \end{aligned} \tag{A.2}$$

The remaining oscillators are unsynchronized, and stationarity requires

$$\begin{aligned} \rho(\Delta, \omega, x) &= \frac{a}{|\dot{\Delta}|} g(\omega) = \frac{a}{\left|\omega - M(x)\sin\Delta\right|} g(\omega), \\ |\omega| &> M(x). \end{aligned} \tag{A.3}$$

with $a$ determined by normalization.

Combining Equation 2.21, Equation A.2, and Equation A.3 yields a self-consistency equation for the order parameter:

$$
\begin{aligned}
R =& I_1 + I_2, \\
I_1 =& \frac{1}{2} \int_{-1}^{1} \mathrm{d}y \int_{0}^{2\pi} \mathrm{d}\Delta \int_{0}^{2\pi} \mathrm{d}\Delta' \int_{-M(|y|)}^{M(|y|)} \mathrm{d}\omega \int_{-M(|y|)}^{M(|y|)} \mathrm{d}\omega' g(\omega) g(\omega') \\
& \times \mathrm{e}^{\mathrm{sgn}(y)\mathrm{i}\Delta} \mathrm{e}^{-\mathrm{sgn}(y)\mathrm{i}\Delta'} \\
& \times \delta\left(\Delta - \arcsin \frac{\omega}{M(|y|)}\right) \delta\left(\Delta' - \arcsin \frac{\omega'}{M(|y|)}\right), \\
I_2 =& \frac{1}{2} \int_{-1}^{1} \mathrm{d}y \int_{0}^{2\pi} \mathrm{d}\Delta \int_{0}^{2\pi} \mathrm{d}\Delta' \int_{|\omega| > M(|y|)} \mathrm{d}\omega \int_{|\omega'| > M(|y|)} \mathrm{d}\omega' g(\omega) g(\omega') \\
& \times \mathrm{e}^{\mathrm{sgn}(y)\mathrm{i}\Delta} \mathrm{e}^{-\mathrm{sgn}(y)\mathrm{i}\Delta'} \\
& \times \frac{a}{\left|\omega - M(|y|) \sin \Delta\right|} \cdot \frac{a}{\left|\omega' - M(|y|) \sin \Delta'\right|}.
\end{aligned}
\tag{A.4}
$$

For even, unimodal $g(\omega)$, Equation A.3 admits a symmetry in $\Delta$ and $\omega$ that causes the integrals over $\omega$ to vanish and so the unlocked oscillators do not contribute to the order parameter (see for example [103]). Evaluating the $\Delta$ integrals, Equation A.4 reduces to

$$
\begin{aligned}
R =& \frac{1}{2} \int_{-1}^{1} \mathrm{d}y \int_{-M(|y|)}^{M(|y|)} \mathrm{d}\omega \int_{-M(|y|)}^{M(|y|)} \mathrm{d}\omega' g(\omega) g(\omega') \\
& \times \exp\left[\mathrm{i}\ \mathrm{sgn}(y) \arcsin \frac{\omega}{M(|y|)}\right] \\
& \times \exp\left[-\mathrm{i}\ \mathrm{sgn}(y) \arcsin \frac{\omega'}{M(|y|)}\right].
\end{aligned}
\tag{A.5}
$$

Expanding the complex exponentials, the imaginary terms are linear in $\omega$ and $\omega'$ respectively and thus vanish upon integration with even $g$. As a result, both integrands are even

in $y$ and Equation A.5 reduces to

$$R = \int_0^1 \mathrm{d}y \left[ \int_{-M(y)}^{M(y)} \mathrm{d}\omega \; g(\omega) \sqrt{1 - \left( \frac{\omega}{M(y)} \right)^2} \right]^2 . \tag{A.6}$$

Taking a change of variables

$$\omega = M(y) \sin\theta, \tag{A.7}$$

we end up with the indicated result

$$\begin{aligned} R &= \int_0^1 \mathrm{d}y \left[ M(y) \int_{-\frac{\pi}{2}}^{\frac{\pi}{2}} \mathrm{d}\theta \; g\big(M(y)\sin\theta\big) \cos^2\theta \right]^2 . \\ &= \int_0^1 \mathrm{d}y \left[ \frac{(2-y)KR}{2} \int_{-\frac{\pi}{2}}^{\frac{\pi}{2}} \mathrm{d}\theta \; g\left[ \frac{(2-y)KR}{2} \sin\theta \right] \cos^2\theta \right]^2 \end{aligned} \tag{A.8}$$

# APPENDIX B

# MODELS AND PARAMETERS FOR CHAPTER 3

We use the formulation of the FHN model presented in [104] with parameters $\alpha = .1$, $\beta = .5$, $\gamma = 1$, $\epsilon = .012$, $\delta = 0$, $D = .001$, domain size $L = 6$, and grid points $N_x = N_y = 200$. Contour and stimulus thresholds are $u_{\text{th}} = .3$, $v_{\text{th}} = .07$, $g_{\text{th}} = .04$. For the thicker spiral wave in Figure 3.2, $\beta = .2$ and $\epsilon = .005$.

The smoothed Karma model and parameters used in Figure 3.6 are given in [48] though we increase the smoothing parameter to $s = 10$. The domain size and grid points are $L = N_x = N_y = 200$. Contour and stimulus thresholds are $u_{\text{th}} = 1.75$, $v_{\text{th}} = .95$, $g_{\text{th}} = .03$.

## REFERENCES


[1] Y. Kuramoto, *Chemical oscillations, waves, and turbulence*, ser. Springer series in synergetics ; v. 19. Berlin ; New York: Springer-Verlag, 1984, ISBN: 0387133224.

[2] A. T. Winfree, *The geometry of biological time*, ser. Biomathematics ; v. 8. 1980, ISBN: 0387093737.

[3] J. J. Tyson and J. P. Keener, "Singular perturbation theory of traveling waves in excitable media (a review)," *Physica. D*, vol. 32, no. 3, pp. 327–361, 1988.

[4] B. Monga, D. Wilson, T. Matchen, and J. Moehlis, "Phase reduction and phase-based optimal control for biological systems: A tutorial," *Biological cybernetics*, vol. 113, no. 1, pp. 11–46, 2019.

[5] D. Margerit and D. Barkley, "Cookbook asymptotics for spiral and scroll waves in excitable media," *Chaos: An Interdisciplinary Journal of Nonlinear Science*, vol. 12, no. 3, pp. 636–649, 2002.

[6] H. Nakao, "Phase reduction approach to synchronisation of nonlinear oscillators," *Contemporary physics*, vol. 57, no. 2, pp. 188–214, 2016.

[7] Y. Kuramoto, "Self-entrainment of a population of coupled non-linear oscillators," in *International Symposium on Mathematical Problems in Theoretical Physics*, H. Araki, Ed., Berlin, Heidelberg: Springer Berlin Heidelberg, 1975, pp. 420–422, ISBN: 978-3-540-37509-8.

[8] K. Wiesenfeld, "Synchronization in disordered superconducting arrays," *Journal of physics. A, Mathematical and theoretical*, vol. 53, no. 6, p. 64 002, 2020.

[9] A. Winfree and S. Strogatz, "Singular filaments organize chemical waves in three dimensions: I. geometrically simple waves," *Physica. D*, vol. 8, no. 1, pp. 35–49, 1983.

[10] M. Cross, *Pattern formation and dynamics in nonequilibrium systems*. Cambridge, UK ; New York: Cambridge University Press, 2009, ISBN: 1-107-19468-7.

[11] A. T. Winfree, *When time breaks down : the three-dimensional dynamics of electrochemical waves and cardiac arrhythmias / Arthur T. Winfree.* Princeton, N.J.: Princeton University Press, 1987, ISBN: 0691084432.

[12] J. Jalife, R. A. Gray, and A. M. Pertsov, "Spatial and temporal organization during cardiac fibrillation," *Nature (London)*, vol. 392, no. 6671, pp. 75–78, 1998.

[13] E. M. Cherry and F. H. Fenton, "Visualization of spiral and scroll waves in simulated and experimental cardiac tissue," *New Journal of Physics*, vol. 10, no. 12, p. 125 016, 2008.

[14] F. H. Fenton, E. M. Cherry, H. M. Hastings, and S. J. Evans, "Multiple mechanisms of spiral wave breakup in a model of cardiac electrical activity," *Chaos: An Interdisciplinary Journal of Nonlinear Science*, vol. 12, no. 3, pp. 852–892, 2002.

[15] O. Mcduff and S. Harris, "Nonlinear theory of the internally loss-modulated laser," *IEEE Journal of Quantum Electronics*, vol. 3, no. 3, pp. 101–111, 1967.

[16] D. Kuizenga and A. Siegman, "Fm and am mode locking of the homogeneous laser - part i: Theory," *IEEE Journal of Quantum Electronics*, vol. 6, no. 11, pp. 694–708, 1970.

[17] M. Sargent, *Laser physics*. Reading, Mass.: Addison-Wesley Pub. Co., Advanced Book Program, 1974, ISBN: 0201067188.

[18] H. A. Haus, "Theory of mode locking with a fast saturable absorber," *Journal of Applied Physics*, vol. 46, no. 7, pp. 3049–3058, 1975.

[19] H. Haus, J. Fujimoto, and E. Ippen, "Structures for additive pulse mode locking," *Journal of the Optical Society of America B: Optical Physics*, vol. 8, no. 10, pp. 2068–2076, 1991.

[20] H. Haus, "Mode-locking of lasers," *IEEE Journal of Selected Topics in Quantum Electronics*, vol. 6, no. 6, pp. 1173–1185, 2000.

[21] O. E. Martinez, R. L. Fork, and J. P. Gordon, "Theory of passively mode-locked lasers including self-phase modulation and group-velocity dispersion.," *Optics letters*, vol. 9, no. 5, pp. 156–158, 1984.

[22] H. Haken, *Light*. Amsterdam ; New York : New York: North-Holland Pub. Co. ; Sole distributors for the U.S.A. and Canada, Elsevier North-Holland, 1981, ISBN: 0444860207.

[23] Y. H. Wen, M. R. E. Lamont, S. H. Strogatz, and A. L. Gaeta, "Self-organization in kerr-cavity-soliton formation in parametric frequency combs," *Physical Review A*, vol. 94, no. 6, Dec. 2016.

[24] H. Taheri, A. A. Eftekhar, K. Wiesenfeld, and A. Adibi, "Anatomy of phase locking in hyperparametric oscillations based on kerr nonlinearity," *IEEE Photonics Journal*, vol. 9, no. 3, pp. 1–11, 2017.

[25] H. Taheri, P. Del'Haye, A. A. Eftekhar, K. Wiesenfeld, and A. Adibi, "Self-synchronization phenomena in the lugiato-lefever equation," *Physical Review A*, vol. 96, no. 1, Jul. 2017.

[26] Lugiato and Lefever, "Spatial dissipative structures in passive optical systems.," *Physical review letters*, vol. 58, no. 21, pp. 2209–2211, 1987.

[27] P. Ashwin and A. Rodrigues, "Hopf normal form with $s_n$ symmetry and reduction to systems of nonlinearly coupled phase oscillators," *Physica D: Nonlinear Phenomena*, vol. 325, pp. 14–24, Jun. 2016.

[28] A. Gushchin, E. Mallada, and A. Tang, "Synchronization of heterogeneous kuramoto oscillators with graphs of diameter two," in *2015 49th Annual Conference on Information Sciences and Systems (CISS)*, Feb. 2015, pp. 1–6.

[29] D. Pazó, "Thermodynamic limit of the first-order phase transition in the kuramoto model," *Physical review. E, Statistical, nonlinear, and soft matter physics*, vol. 72, no. 4 Pt 2, Oct. 2005.

[30] S. Gupta, "Spontaneous collective synchronization in the Kuramoto model with additional non-local interactions," *Journal of Physics A Mathematical General*, vol. 50, 424001, p. 424 001, Oct. 2017.

[31] S. H. ( H. Strogatz, *Nonlinear dynamics and Chaos : with applications to physics, biology, chemistry, and engineering*, ser. Studies in nonlinearity. Reading, Mass.: Addison-Wesley Pub., 1994, ISBN: 0201543443.

[32] E. Ott and T. M. Antonsen, "Low dimensional behavior of large systems of globally coupled oscillators," *Chaos: An Interdisciplinary Journal of Nonlinear Science*, vol. 18, no. 3, p. 037 113, 2008. eprint: https://doi.org/10.1063/1.2930766.

[33] S. H. Strogatz, "From kuramoto to crawford: Exploring the onset of synchronization in populations of coupled oscillators," *Phys. D*, vol. 143, no. 1-4, pp. 1–20, Sep. 2000.

[34] A. T. Winfree, "Spiral waves of chemical activity," *Science*, vol. 175, no. 4022, pp. 634–636, 1972.

[35] G. Kastberger, E. Schmelzer, and I. Kranner, "Social waves in giant honeybees repel hornets," *PLoS One*, vol. 3, no. 9, e3141, 2008.

[36] J. J. Tyson, K. A. Alexander, V. Manoranjan, and J. Murray, "Spiral waves of cyclic amp in a model of slime mold aggregation," *Physica D: Nonlinear Phenomena*, vol. 34, no. 1-2, pp. 193–207, 1989.

[37] K. Tsuji and S. C. Müller, *Spirals and Vortices*. Springer, 2019.

[38] J. M. Davidenko, A. V. Pertsov, R. Salomonsz, W. Baxter, and J. Jalife, "Stationary and drifting spiral waves of excitation in isolated cardiac muscle," *Nature*, vol. 355, no. 6358, pp. 349–351, 1992.

[39] M. S. Eisenberg, "Defibrillation: The spark of life," *Scientific American*, vol. 278, no. 6, pp. 86–91, 1998.

[40] D. J. Dosdall, V. G. Fast, and R. E. Ideker, "Mechanisms of defibrillation," *Annual review of biomedical engineering*, vol. 12, no. 1, pp. 233–258, 2010.

[41] R. E. Ideker, T. N. Chattipakorn, and R. A. Gray, "Defibrillation mechanisms: The parable of the blind men and the elephant," *Journal of cardiovascular electrophysiology*, vol. 11, no. 9, pp. 1008–1013, 2000.

[42] F. H. Fenton, S. Luther, E. M. Cherry, N. F. Otani, V. Krinsky, A. Pumir, E. Bodenschatz, and R. F. Gilmour Jr, "Termination of atrial fibrillation using pulsed low-energy far-field stimulation," *Circulation*, vol. 120, no. 6, p. 467, 2009.

[43] I. R. Efimov, Y. Cheng, D. R. Van Wagoner, T. Mazgalev, and P. J. Tchou, "Virtual electrode–induced phase singularity: A basic mechanism of defibrillation failure," *Circulation Research*, vol. 82, no. 8, pp. 918–925, 1998.

[44] W. Li, A. H. Janardhan, V. V. Fedorov, Q. Sha, R. B. Schuessler, and I. R. Efimov, "Low-energy multistage atrial defibrillation therapy terminates atrial fibrillation with less energy than a single shock," *Circulation: Arrhythmia and Electrophysiology*, vol. 4, no. 6, pp. 917–925, 2011.

[45] S. Luther, F. H. Fenton, B. G. Kornreich, A. Squires, P. Bittihn, D. Hornung, M. Zabel, J. Flanders, A. Gladuli, L. Campoy, E. M. Cherry, G. Luther, G. Hasenfuss, V. I. Krinsky, A. Pumir, R. F. Gilmour, and E. Bodenschatz, "Low-energy control of electrical turbulence in the heart," *Nature (London)*, vol. 475, no. 7355, pp. 235–239, 2011.

[46] R. A. Gray, N. Chattipakorn, and H. L. Swinney, "Termination of spiral waves during cardiac fibrillation via shock-induced phase resetting," *Proceedings of the National Academy of Sciences - PNAS*, vol. 102, no. 13, pp. 4672–4677, 2005.

[47] D. Wilson and J. Moehlis, "Toward a more efficient implementation of antifibrillation pacing," *PloS one*, vol. 11, no. 7, e0158239, 2016.

[48] C. D. Marcotte and R. O. Grigoriev, "Dynamical mechanism of atrial fibrillation: A topological approach," *Chaos (Woodbury, N.Y.)*, vol. 27, no. 9, p. 093 936, 2017.

[49] J. P. Keener, "The topology of defibrillation," *Journal of theoretical biology*, vol. 230, no. 4, pp. 459–473, 2004.

[50] R. FitzHugh, "Impulses and physiological states in theoretical models of nerve membrane," *Biophysical journal*, vol. 1, no. 6, p. 445, 1961.

[51] A. Karma, "Spiral breakup in model equations of action potential propagation in cardiac tissue," *Physical review letters*, vol. 71, no. 7, p. 1103, 1993.

[52] A. N. Iyer and R. A. Gray, "An experimentalist's approach to accurate localization of phase singularities during reentry," *Annals of biomedical engineering*, vol. 29, no. 1, pp. 47–59, 2001.

[53] J. Beaumont, N. Davidenko, J. M. Davidenko, and J. Jalife, "Spiral waves in two-dimensional models of ventricular muscle: Formation of a stationary core," *Biophysical journal*, vol. 75, no. 1, pp. 1–14, 1998.

[54] F. Fenton and A. Karma, "Vortex dynamics in three-dimensional continuous myocardium with fiber rotation: Filament instability and fibrillation," *Chaos: An Interdisciplinary Journal of Nonlinear Science*, vol. 8, no. 1, pp. 20–47, 1998.

[55] D. R. Gurevich and R. O. Grigoriev, "Robust approach for rotor mapping in cardiac tissue," *Chaos (Woodbury, N.Y.)*, vol. 29, no. 5, p. 053 101, 2019.

[56] D. R. Gurevich, C. Herndon, I. Uzelac, F. H. Fenton, and R. O. Grigoriev, "Level-set method for robust analysis of optical mapping recordings of fibrillation," *Computing in Cardiology*, vol. 44, pp. 197–427, 2017.

[57] N. D. Mermin, "The topological theory of defects in ordered media," *Reviews of modern physics*, vol. 51, no. 3, pp. 591–648, 1979.

[58] J. Davidsen, L. Glass, and R. Kapral, "Topological constraints on spiral wave dynamics in spherical geometries with inhomogeneous excitability," *Physical Review E*, vol. 70, no. 5, p. 056 203, 2004.

[59] A. M. Pertsov, M. Wellner, M. Vinson, and J. Jalife, "Topological constraint on scroll wave pinning," *Physical review letters*, vol. 84, no. 12, p. 2738, 2000.

[60] F. Siso-Nadal, N. F. Otani, R. F. Gilmour Jr, and J. J. Fox, "Boundary-induced reentry in homogeneous excitable tissue," *Physical review. E, Statistical, nonlinear, and soft matter physics*, vol. 78, no. 3 Pt 1, pp. 031 925–031 925, 2008.

[61] A. M. Pertsov, J. M. Davidenko, R. Salomonsz, W. T. Baxter, and J. Jalife, "Spiral waves of excitation underlie reentrant activity in isolated cardiac muscle," *Circulation research*, vol. 72, no. 3, pp. 631–650, 1993.

[62] D. W. Frazier, P. D. Wolf, J. M. Wharton, A. S. L. Tang, W. M. Smith, and R. E. Ideker, "Stimulus-induced critical point: Mechanism for electrical initiation of reentry in normal canine myocardium," *The Journal of clinical investigation*, vol. 83, no. 3, pp. 1039–1052, 1989.

[63] A. Pumir and V. I. Krinsky, "Two biophysical mechanisms of defibrillation of cardiac tissue," *Journal of theoretical biology*, vol. 185, no. 2, pp. 189–199, 1997.

[64] ——, "How does an electric field defibrillate cardiac muscle?" *Physica. D*, vol. 91, no. 1, pp. 205–219, 1996.

[65] G. W. Beeler and H. Reuter, "Reconstruction of the action potential of ventricular myocardial fibres," *The Journal of physiology*, vol. 268, no. 1, pp. 177–210, 1977.

[66] K. H. ten Tusscher, D. Noble, P.-J. Noble, and A. V. Panfilov, "A model for human ventricular tissue," *American Journal of Physiology-Heart and Circulatory Physiology*, vol. 286, no. 4, H1573–H1589, 2004.

[67] T. O'Hara, L. Virág, A. Varró, and Y. Rudy, "Simulation of the undiseased human cardiac ventricular action potential: Model formulation and experimental validation," *PLoS Comput Biol*, vol. 7, no. 5, e1002061, 2011.

[68] A. Kaboudian, E. M. Cherry, and F. H. Fenton, "Real-time interactive simulations of large-scale systems on personal computers and cell phones: Toward patient-specific heart modeling and other applications," *Science advances*, vol. 5, no. 3, eaav6019, 2019.

[69] A. Kaboudian, Defibrillation by Teleportation, https://kaboudian.github.io/DefibrillationByTelepor

[70] N. Chattipakorn, I. Banville, R. A. Gray, and R. E. Ideker, "Effects of shock strengths on ventricular defibrillation failure," *Cardiovascular research*, vol. 61, no. 1, pp. 39–44, 2004.

[71] I. R. Efimov, Y. Cheng, Y. Yamanouchi, and P. J. Tchou, "Direct evidence of the role of virtual electrode-induced phase singularity in success and failure of defibrillation," *Journal of cardiovascular electrophysiology*, vol. 11, no. 8, pp. 861–868, 2000.

[72] C. Crocini, C. Ferrantini, R. Coppini, M. Scardigli, P. Yan, L. M. Loew, G. Smith, E. Cerbai, C. Poggesi, F. S. Pavone, and L. Sacconi, "Optogenetics design of mechanistically-based stimulation patterns for cardiac defibrillation," *Scientific reports*, vol. 6, no. 1, pp. 35 628–35 628, 2016.

[73] R. A. B. Burton, A. Klimas, C. M. Ambrosi, J. Tomek, A. Corbett, E. Entcheva, and G. Bub, "Optical control of excitation waves in cardiac tissue," *Nature photonics*, vol. 9, no. 12, pp. 813–816, 2015.

[74] T. Bánsági and O. Steinbock, "Three-dimensional spiral waves in an excitable reaction system: Initiation and dynamics of scroll rings and scroll ring pairs," *Chaos: An Interdisciplinary Journal of Nonlinear Science*, vol. 18, no. 2, p. 026 102, 2008.

[75] A. Pumir, V. Nikolski, M. Hörning, A. Isomura, K. Agladze, K. Yoshikawa, R. Gilmour, E. Bodenschatz, and V. Krinsky, "Wave emission from heterogeneities opens a way to controlling chaos in the heart," *Physical review letters*, vol. 99, no. 20, pp. 208 101–208 101, 2007.

[76] P. Buran, M. Bär, S. Alonso, and T. Niedermayer, "Control of electrical turbulence by periodic excitation of cardiac tissue," *Chaos (Woodbury, N.Y.)*, vol. 27, no. 11, pp. 113 110–113 110, 2017.

[77] C. M. Ambrosi, C. M. Ripplinger, I. R. Efimov, and V. V. Fedorov, "Termination of sustained atrial flutter and fibrillation using low-voltage multiple-shock therapy," *Heart Rhythm*, vol. 8, no. 1, pp. 101–108, 2011.

[78] Y. C. Ji, P. Uzelac Ilija, P. Otani Niels, P. Luther Stefan, P. Gilmour Robert F., P. Cherry Elizabeth M., and P. Fenton Flavio H., "Synchronization as a mechanism for low-energy anti-fibrillation pacing (leap)," *Heart rhythm*, vol. 14, no. 8, pp. 1254–1262, 2017.

[79] J. M. Greenberg and S. P. Hastings, "Spatial patterns for discrete models of diffusion in excitable media," *SIAM Journal on Applied Mathematics*, vol. 34, no. 3, pp. 515–523, 1978.

[80] J. Greenberg, C. Greene, and S. Hastings, "A combinatorial problem arising in the study of reaction-diffusion equations," *SIAM Journal on Algebraic Discrete Methods*, vol. 1, no. 1, pp. 34–42, 1980.

[81] G. P. Walcott, C. R. Killingsworth, and R. E. Ideker, "Do clinically relevant transthoracic defibrillation energies cause myocardial damage and dysfunction?" *Resuscitation*, vol. 59, no. 1, pp. 59–70, 2003.

[82] I. R. Efimov, Y. Cheng, D. R. Van Wagoner, T. Mazgalev, and P. J. Tchou, "Virtual electrode–induced phase singularity: A basic mechanism of defibrillation failure," *Circulation Research*, vol. 82, no. 8, pp. 918–925, 1998.

[83] F. H. Fenton, S. Luther, E. M. Cherry, N. F. Otani, V. Krinsky, A. Pumir, E. Bodenschatz, and R. F. Gilmour Jr, "Termination of atrial fibrillation using pulsed low-energy far-field stimulation," *Circulation*, vol. 120, no. 6, p. 467, 2009.

[84] I. R. Efimov, Y. Cheng, D. R. Van Wagoner, T. Mazgalev, and P. J. Tchou, "Virtual electrode-induced phase singularity: A basic mechanism of defibrillation failure," *Circulation research*, vol. 82, no. 8, pp. 918–925, 1998.

[85] Szabó and Ódor, "Extended mean-field study of a stochastic cellular automaton.," *Physical review. E, Statistical physics, plasmas, fluids, and related interdisciplinary topics*, vol. 49, no. 4, pp. 2764–2768, 1994.

[86] D. Hiebeler, "Stochastic spatial models: From simulations to mean field and local structure approximations," *Journal of Theoretical Biology*, vol. 187, no. 3, pp. 307–319, 1997.

[87] K. L. P, *Statistical Physics: Statics, Dynamics And Renormalization*. Singapore: World Scientific Publishing Company, 2000, ISBN: 9789810237585.

[88] N. DeTal and F. Fenton, "Terminating spiral waves with a single designed stimulus: Teleportation as the mechanism for defibrillation," *Physical review letters*, Under review.

[89] J. Bragard, A. Simic, J. Elorza, R. O. Grigoriev, E. M. Cherry, R. F. Gilmour, N. F. Otani, and F. H. Fenton, "Shock-induced termination of reentrant cardiac arrhythmias: Comparing monophasic and biphasic shock protocols," *Chaos (Woodbury, N.Y.)*, vol. 23, no. 4, pp. 043 119–043 119, 2013.

[90] P. Buran and M. Bär, Private Communication, 2021.

[91] V. N. Biktashev, A. V. Holden, H. Zhang, J. Brindley, and P. Gray, "Tension of organizing filaments of scroll waves," *Philosophical Transactions of the Royal Society of London. Series A: Physical and Engineering Sciences*, vol. 347, no. 1685, pp. 611–630, 1994.

[92] S. Alonso, M. Bär, and A. V. Panfilov, "Negative tension of scroll wave filaments and turbulence in three-dimensional excitable media and application in cardiac dynamics," *Bulletin of mathematical biology*, vol. 75, no. 8, pp. 1351–1376, 2013.

[93] B. Bezekci, I. Idris, R. D. Simitev, and V. N. Biktashev, "Semianalytical approach to criteria for ignition of excitation waves," *Physical review. E, Statistical, nonlinear, and soft matter physics*, vol. 92, no. 4, pp. 042 917–042 917, 2015.

[94] C. D. Marcotte and V. N. Biktashev, "Predicting critical ignition in slow-fast excitable models," *Physical review. E*, vol. 101, no. 4-1, pp. 042 201–042 201, 2020.

[95] E. N. Cytrynbaum and T. J. Lewis, "A global bifurcation and the appearance of a one-dimensional spiral wave in excitable media," *SIAM journal on applied dynamical systems*, vol. 8, no. 1, pp. 348–370, 2009.

[96] X. Cabré, E. Fontich, and R. de la Llave, "The parameterization method for invariant manifolds iii: Overview and applications," *Journal of Differential Equations*, vol. 218, no. 2, pp. 444–515, 2005.

[97] À. Haro, M. Canadell, A. Luque, J. M. Mondelo, and J.-L. Figueras, *The Parameterization Method for Invariant Manifolds: From Rigorous Results to Effective Computations*, ser. Applied Mathematical Sciences. Cham: Springer International Publishing AG, 2016, vol. 195, ISBN: 3319296604.

[98] E. N. Cytrynbaum and K. M. Paton, "An invariant winding number for the fitzhugh–nagumo system with applications to cardiac dynamics," *SIAM journal on applied dynamical systems*, vol. 16, no. 4, pp. 1893–1922, 2017.

[99] E. Ermakova and A. Pertsov, "Interaction of rotating spiral waves with a boundary," *Biofizika*, vol. 31, no. 5, pp. 855–861, 1986.

[100] C. D. Marcotte and R. O. Grigoriev, "Adjoint eigenfunctions of temporally recurrent single-spiral solutions in a simple model of atrial fibrillation," *Chaos: An Interdisciplinary Journal of Nonlinear Science*, vol. 26, no. 9, p. 093 107, 2016.

[101] M. Aron, S. Herzog, U. Parlitz, S. Luther, and T. Lilienkamp, "Spontaneous termination of chaotic spiral wave dynamics in human cardiac ion channel models," *PloS one*, vol. 14, no. 8, e0221401, 2019.

[102] T. Lilienkamp and U. Parlitz, "Terminating transient chaos in spatially extended systems," *Chaos: An Interdisciplinary Journal of Nonlinear Science*, vol. 30, no. 5, p. 051 108, 2020.

[103] S. H. Strogatz, "Norbert wiener's brain waves," in *Frontiers in Mathematical Biology*, S. A. Levin, Ed., Berlin, Heidelberg: Springer Berlin Heidelberg, 1994, pp. 122–138, ISBN: 978-3-642-50124-1.

[104] Y. C. Ji and F. H. Fenton, "Numerical solutions of reaction-diffusion equations: Application to neural and cardiac models," *American journal of physics*, vol. 84, no. 8, pp. 626–638, 2016.